

# Propulsion of flapping foils undergoing in-plane clap-and-fling and deviation motions

Antoine Papillon<sup>a,1</sup>, Mathieu Olivier<sup>a,2,\*</sup>

<sup>a</sup>*Department of Mechanical Engineering, Université Laval, Quebec City, QC, G1V 0A6, Canada*

---

## Abstract

This study examines the performance of two flapping flat-plate foils interacting with each other while generating thrust at a Reynolds number of 800 through two-dimensional numerical simulations. These fluid dynamics simulations were conducted with a commercial computational fluid dynamics solver implementing a finite-volume method and an overset mesh capability. The foils performed a combined motion involving pitching, heaving, and deviation. Both foils exhibit similar movements, with one foil mirroring the other. The heaving and pitching motions occur at the same frequency but with a phase shift between them. The effects of varying the phase shift and the minimum spacing between the foils during motion were first explored. The study revealed that a maximum efficiency of 0.542 can be achieved by using two foils, representing an increase of 13.5% relative to the optimal single-foil case. Then, the impacts of the deviation motion were investigated. The deviation motion was introduced with a frequency twice as fast as the other motions, and a phase shift relative to the heaving motion. The other parameters such as the minimum spacing between the foils, the heaving and pitching amplitudes, and the frequency were those of the best configuration without deviation. The numerical simulations demonstrated that deviation can increase efficiency further to a value of 0.560, a relative increase of 3.95%.

*Keywords:* flapping foils, deviation, propulsion, clap and fling, low Reynolds number

---

## 1. Introduction

The pursuit of leveraging useful aerodynamic forces from fluid flows has captured the interest of researchers throughout the years. Numerous studies have investigated flapping wings to either generate thrust or extract energy from such flows (Tuncer and Platzer, 1999; Anderson et al., 1998; Miller and Peskin, 2005; Wu et al., 2020). This concept draws inspiration from the efficient aerodynamics observed in various species of insects and small birds that continuously flap their wings at specific frequencies to achieve flight. This approach contrasts with intermittent flapping and gliding, a technique used by most larger birds subject to larger Reynolds numbers. In some cases, an

---

\*Corresponding author

*Email address:* mathieu.olivier@gmc.ulaval.ca (Mathieu Olivier)

<sup>1</sup>antoine.papillon.1@ulaval.ca

<sup>2</sup>mathieu.olivier@gmc.ulaval.ca

intriguing phenomenon known as clap and fling is used. This mechanism was initially reported by Weis-Fogh (1973) who studied the flight of the diminutive wasp *Encarsia formosa*. They also demonstrated that this clap-and-fling mechanism has been adopted by some birds and insects for flight. It involves wings coming into proximity during flapping, resulting in enhanced thrust or lift generation through their interaction.

Conventional aerodynamic theories have often fallen short in explaining how sufficient lift is generated at low Reynolds numbers, particularly for hovering. Earlier studies identified that unsteady mechanisms play a crucial role in this matter (Ansari et al., 2006; Dickinson et al., 1999; Ellington et al., 1996). Among them, the clap-and-fling mechanism, illustrated in Figure 1, has been widely studied for its efficient circulation generation around flapping wings through mutual interaction. During the clap phase, the wings move toward each other and nearly touch. This is followed by the fling phase, where the wings separate, inducing circulation that rapidly reaches a steady state (Lighthill, 1973). Unlike traditional steady-state aerodynamics, this mechanism bypasses the need for the Kutta condition to establish circulation. The rapid reach of steady circulation allows the wings to maximize lift during each oscillation cycle, explaining why several species evolved to use this mechanism for flight at lower Reynolds numbers.

Building on these biological insights, computational and experimental studies have advanced the understanding of flapping-wing aerodynamics. Platzer et al. (1993) analyzed thrust and lift in oscillating airfoils using a panel code, revealing the impact of unsteady forces. Later work by Tuncer and Platzer (1999) introduced a Navier-Stokes solver to account for flow separation and wake profiles, highlighting the role of attached flows in achieving higher propulsive efficiencies. At higher plunging frequencies, leading-edge vortices were observed to generate more thrust but at the cost of reduced efficiency. These insights have inspired biomimetic designs, such as developing flapping-wing vehicles with features mimicking species at comparable Reynolds numbers (Jones and Platzer, 2009). Such designs leverage unsteady aerodynamic advantages, including ground effects and wake ingestion, to optimize thrust and efficiency (Platzer et al., 2008), underscoring the continued relevance of biological flight mechanics to engineering innovation.

Meanwhile, numerous studies about flapping wings revealed the importance of kinematic parameters on aerodynamic performances. In the case of harmonic wing motions involving clap and fling, the phase shift between the heaving and pitching movements has a significant impact since it controls the kinematics of the foils when they reach proximity. For single harmonically flapping foils, the optimal phase shift depends on the location of the pivot point on the oscillating foil. Anderson et al. (1998) have shown that this optimal phase shift when the pivot point is at one-third of the chord length is  $75^\circ$ . They also pointed out that changing the pivot point location has similar effects to modifying the phase shift in the case of small amplitude motions. This is also supported by Isogai et al. (1999), who found that the optimal efficiency occurs at a phase shift of  $90^\circ$  when the pivot point is located at the middle of the chord length.

The impact of the interactions between two foils undergoing clap-and-fling motion has been examined by some authors with two-dimensional numerical simulations (Mao and Xin, 2003; Miller and Peskin, 2005; Zhu and Lei, 2018). In the work by Mao and Xin (2003), a hovering configuration with a Reynolds number of 17 and a motion described by piecewise-continuous functions is used. This configuration corresponds to the kinematics and physical scales of a wasp (*Encarsia Formosa*). They reported that reducing the minimum spacing between the foils increases

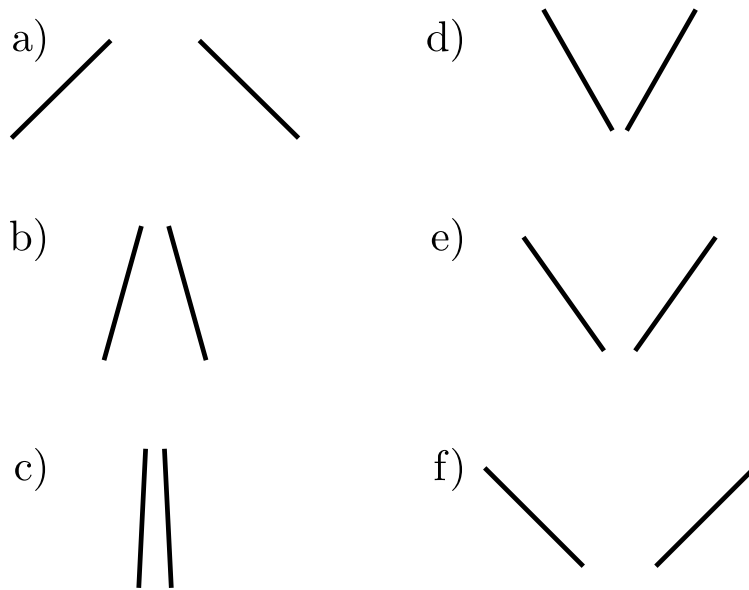


Figure 1: Schematic of wing sections during clap (a-c) and fling (d-f). The motion occurs sequentially from (a) to (f) and the generated force is upward.

the lift coefficient. Yet, the moment coefficient, which is directly related to the necessary power that needs to be injected to accomplish the motion, increases significantly as the foils are closer initially. Mao and Xin (2003) discussed that when the initial spacing varies between the smallest values considered (10 to 20 percent of the chord length), the lift coefficient barely diminishes while the moment coefficient becomes much smaller. Hence, a compromise has to be made when setting the initial spacing to maximize the lift while minimizing the power required to execute the motion. They have also reported strong lift peaks during the clap phase, which correspond to the moment when the trailing edges of the foils are close to each other. They concluded that the clap-and-fling interaction can increase the lift coefficient by a factor of up to 1.6 when compared to single foils. This confirms, to some extent, that this mechanism can significantly improve lift.

Subsequently, Miller and Peskin (2005) determined that a lower Reynolds number could increase the lift of heaving and pitching foils. The spacing between the two foils at the end of the fling movement was specified as  $1/6$  of the chord length, which allows proximity effects to occur. Their simulations were carried out for Reynolds numbers between 8 and 128. At lower Reynolds numbers, lift improvements were reported during the translation and rotation phases of the motion when compared to a single foil undergoing the same movement. At higher Reynolds numbers, the propulsion improvements were significantly reduced but kept a slight increase during the rotation part of the motion. On the other hand, Miller and Peskin (2005) also showed that the necessary force to sustain the rotation motion increased at lower Reynolds numbers. This implies that small insects likely need to provide significant effort to rotate their wings. It was thus hypothesized that the use of flexible wings could, however, decrease the negative impact of these drag forces at lower Reynolds numbers.

Along the same lines, Zhu and Lei (2018) investigated the effects of proximity and phase difference between the pitching and heaving of two harmonically flapping foils. They considered a system moving with a Reynolds number of  $10^4$  rather than hovering. They reported a 77% increase in thrust and a 46% increase in efficiency under different conditions. The best thrust and efficiency were both obtained when the mean spacing between the foils was 1.4 times the chord length, resulting in a minimum spacing between the foils of about 30 percent of the chord length.

A study by Wang et al. (2004) investigated unsteady effects and compared 2D computations with 3D experiments of different kinematic patterns for a flapping wing in a hovering configuration. A dynamically scaled robotic fly was used to obtain force and flow data experimentally, while a Navier-Stokes solver was employed for the 2D simulations. The wing motion was harmonic and thus followed a sinusoidal flapping and pitching motion. In the experimental case, this motion was confined to an arc about the wing root, while in the 2D computations, a simplification was considered such that the motion was along a straight line. The main results of this study revealed that the force coefficients have a weak dependence on stroke amplitude in the range considered, which was 3-5 times the chord length. However, the forces were shown to be quite sensitive to the phase between the flapping and pitching motions, which is consistent with results from Dickinson et al. (1999). This can be explained by the orientation of the wing at reversal which can optimally benefit from the delayed stall mechanism. This increases the circulation around the wing and consequently increases lift. However, Wang et al. (2004) mentioned that three-dimensional effects reported experimentally have an important role in this mechanism.

Additionally, while numerous studies are based on harmonic motions, real fruit flies benefiting from the clap-and-fling mechanism employ slightly more complex kinematics. A comparison of several wing kinematic models based on 2D Navier-Stokes simulations were performed by Bos et al. (2008) to assess the aerodynamic performances of a hovering insect. A harmonic model, a so-called Robofly model based on the experimental device from Dickinson et al. (1999), a simplified fruit fly model, and a realistic fruit fly model were considered at a Reynolds number of 110. These four models were subjected to different stroke patterns (heaving), angle of attack (pitching), and deviation, a motion of the wing transverse to the main stroke motion. In the first two models, deviation is not used while it is symmetric in the simplified fruit fly model and asymmetric in the realistic fruit fly model. Including deviation results in a figure-of-eight pattern of the wing as viewed by an external observer. The study shows that the mean drag at comparable lift for the harmonic and Robofly models is substantially higher than in more realistic fruit fly models due to their higher effective angle of attack. Bos et al. (2008) also reported that deviation could introduce an important velocity component perpendicular to the stroke, which greatly affects the effective angle of attack of the wings. Although the mean lift and drag were almost unaffected by deviation, their amplitudes decreased. Therefore, the deviation motion levels the force variations, which could be desirable for application to micro air vehicles using such wing kinematics.

Additionally, wing kinematics of free-flying fruit flies were investigated experimentally by Fry et al. (2003) where three-dimensional infrared high-speed videos were taken during the flight maneuvers. As recorded in this study, the flight characteristics of real fruit flies include the deviation motion responsible for the figure-of-eight pattern, the typical wing stroke (heave in 2D), and the pitching motion. The data demonstrates that each motion component is

essentially harmonic except for the pitching motion exhibiting more asymmetry. The most important takeaway of this study is that the deviation motion is essentially in phase with the stroke motion at a frequency twice as high. Furthermore, the data presents these harmonic motions as angular displacements around the root of the three-dimensional wing. In a 2D representation, these angular displacements would thus have a corresponding simplified displacement.

Deviation has also been studied through three-dimensional numerical simulations carried out by Jung et al. (2024). They considered a single flapping wing in a hovering configuration with a similar motion to that of a mosquito, which does not employ the clap-and-fling mechanism. Results demonstrated that for a wing motion with a small sweeping amplitude (which is the wing displacement around its root in 3D), the figure-of-eight pattern resulting from the deviation significantly modified the effective angle of attack during a cycle of motion and thus increased the mean lift by 30%.

In this context, our study aims to explore further the clap-and-fling mechanism of two flapping foils operating in a two-dimensional traveling configuration. Contrary to hovering flight, this configuration implies an incoming flow corresponding to the system velocity. The study focuses on the effects of the phase difference between the heaving and the pitching motions as well as on the minimum spacing between the foils. Our study thus extends the work of Zhu and Lei (2018) as we explore different parameters. In particular, we use a larger flapping amplitude and investigate configurations with near-contact distances between the foils using an overset-mesh technique, resulting in better thrust and efficiency. Furthermore, our study also incorporates the deviation motion into the overall motion of the wings to determine if beneficial effects can be obtained in cases with two wings in proximity. To determine the optimal deviation for a two-dimensional motion, we modified the phase shift between the heaving and deviation components of the motion, as well as the amplitude of the deviation. By comparing the results obtained through the inclusion of deviation to those previously obtained without the latter, we investigate whether incorporating deviation can also lead to higher levels of efficiency and thrust. These performances are also compared against those of a single foil undergoing the baseline heaving and pitching motions. This paper is divided as follows. Firstly, Section 2 presents the numerical methodology and the metrics that characterize the performances of the airfoils. Section 3 presents the verifications of the numerical simulations. Lastly, Section 4 reports and discusses the numerical results obtained with and without deviation.

## **2. Methodology**

### *2.1. Problem definition*

This study employs two-dimensional numerical simulations of a pair of flapping wings to investigate the combined effect of the deviation motion and the clap-and-fling mechanism. By focusing on an in-plane motion, we can explore its unique properties without considering 3D effects, which would require substantial computational resources. Furthermore, considering that natural flapping-wing flyers typically have thin wings and operate at low Reynolds numbers, the impact of wing profile geometry is not significant in the proposed study. Thus, the thin-plate geometry

shown in Figure 2 is used as a foil where  $c$  is the chord length,  $e$  is the plate thickness, and  $x_P$  represents the pivot point distance from the leading edge.

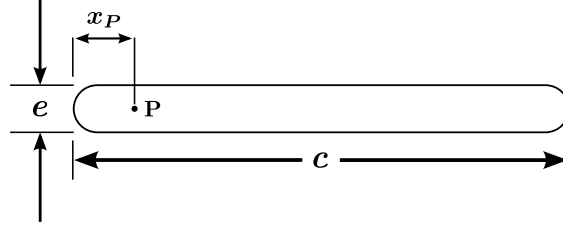


Figure 2: Geometry of a thin flat plate with rounded edges used as a foil.

The motion of the oscillating foils comprises three components: a vertical translation (heaving motion), a rotation (pitching motion), and a horizontal translation (deviation motion). Both foils undergo a symmetric motion as shown in Figure 3, and the motion of the upper foil is described by:

$$h = h_0 \sin(2\pi ft), \quad (1)$$

$$\theta = \theta_0 \sin(2\pi ft - \phi), \quad (2)$$

$$l = l_0 \sin(4\pi ft - \psi), \quad (3)$$

where the heaving, pitching, and deviation amplitudes are denoted by  $h_0$ ,  $\theta_0$ , and  $l_0$ , respectively, and the motion frequency is represented by  $f$ . Lastly,  $\phi$  and  $\psi$  are the phase differences between the heaving motion and the pitching and deviation motions respectively. The complete motion of the two flapping foils is illustrated in Figure 3, where the distance  $d$  represents the minimum spacing attained between the foils throughout the motion cycle. The incoming flow velocity, denoted as  $U_\infty$ , corresponds to the baseline horizontal velocity of the system without considering the effects of the deviation motion.

## 2.2. Parametric Space

The relevant reference scales used for this problem are the length scale  $c$ , the velocity scale  $U_\infty$ , the time scale  $1/f$ , and the pressure scale  $\rho U_\infty^2$ . With these scales, the following dimensionless parameters that govern the problem are obtained:

$$\begin{aligned} Re &= \frac{U_\infty c}{\nu}, & f^* &= \frac{f c}{U_\infty}, & h^* &= \frac{h_0}{c}, & l^* &= \frac{l_0}{c}, \\ e^* &= \frac{e}{c}, & x_P^* &= \frac{x_P}{c}, & d^* &= \frac{d}{c}, & \theta_0, \phi, \psi &. \end{aligned} \quad (4)$$

These parameters are respectively the Reynolds number, the reduced frequency, the normalized heaving amplitude, the normalized deviation amplitude, the relative thickness of the airfoil, the normalized pivot point position, the normalized minimum spacing between the foils, the pitching amplitude, the phase shift between heaving and pitching,

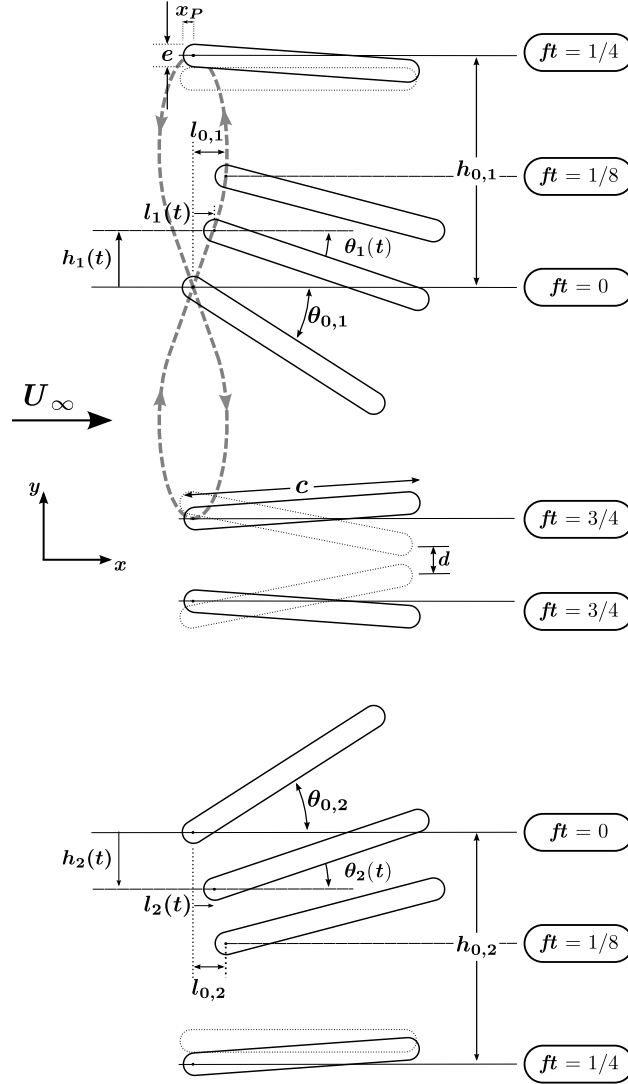


Figure 3: Motion of the two foils ( $\phi = 105^\circ$ ,  $\psi = 0^\circ$ ).

and the phase shift between heaving and deviation. To focus on specific parameters, the following values are fixed throughout the parametric study.

$$Re = 800, \quad h^* = 1, \quad e^* = 0.01, \quad x_p^* = 0.005, \quad \theta_0 = 30^\circ, \quad f^* = 0.15. \quad (5)$$

The Reynolds number is determined based on typical characteristics of flying species presented in Table 1. The choices for normalized heaving amplitude  $h^*$  and normalized pivot point position  $x_p^*$  are somewhat arbitrary but enable the reproduction of a 2D motion resembling that of a mid-span wing section. The pivot point position is essentially located at the leading edge, which is inspired by birds' wings whose motion is driven by the forelimbs. The motion parameters  $f^*$  and  $\theta_0$  are selected to achieve the best efficiency configuration when using a single wing with a phase parameter  $\phi = 90^\circ$  (Olivier and Dumas (2016)). These parameter choices leave the phase shift  $\phi$  and the normalized minimum

Table 1: Flight characteristics of some flying species compiled from various sources (Azuma, 2006; Tobalske et al., 2007; Weis-Fogh, 1973). Dimensionless numbers  $f^*$  and  $Re$  are computed with the largest values of  $U_\infty$ .

Specie	Mass (kg)	$f$ (Hz)	Span (m)	$c$ (m)	$U_\infty$ (m/s)	$f^*$	$Re$
Fruit fly ( <i>Drosophila virilis</i> )	$2 \times 10^{-6}$	240	0.006	0.0015	0 – 0.65	0.55	$6.5 \times 10^1$
Mosquito ( <i>Aedes nearcticus</i> )	$3.5 \times 10^{-6}$	320	0.0054	0.00067	0 – 1.0	0.214	$4.4 \times 10^1$
Bee ( <i>Bombus terrestris</i> )	$8.8 \times 10^{-4}$	156	0.0346	0.0073	0 – 2.41	0.473	$1.2 \times 10^3$
Hummingbird ( <i>Selasphorus rufus</i> )	$3.4 \times 10^{-3}$	41	0.109	0.012	0 – 12	0.041	$9.6 \times 10^3$

spacing between the foils  $d^*$  as the main parameters of interest when no deviation is used. While the normalized distance  $d^*$  certainly affects the clap-and-fling mechanism, the phase shift  $\phi$  influences the timing of the kinematics when both wings come close together, which turns out to have a significant effect as well. The two remaining key parameters in this study are the phase shift  $\psi$  and the normalized deviation amplitude  $l^*$ . The normalized deviation amplitude modulates the deviation motion relative to the heaving and pitching motions, while the phase shift  $\psi$  directly influences the shape of the figure-of-eight pattern. The baseline phase shift considered is  $\psi = 0^\circ$ , corresponding to the experimental flight data collected by Fry et al. (2003).

### 2.3. Performance metrics

The flapping-foil pair illustrated in Figure 3 moves horizontally with the deviation velocity  $\dot{l}$ . The foils's relative velocity with respect to the flow is thus  $U_\infty - \dot{l}$ . When the foils translate horizontally to the left, the effective velocity is thus greater than the nominal velocity  $U_\infty$  while the opposite occurs when the foils translate to the right. Furthermore, each foil is subject to the aerodynamic force ( $F_x, F_y$ ) and aerodynamic moment  $M_P$ . Considering the proposed orientation for the  $x$  and  $y$  axes, the net thrust force which takes into account the required force to perform the deviation motion is  $-F_x$  while  $F_y$  and  $M_P$  are the force and moment required to sustain the flapping motion of each foil. The instantaneous thrust coefficient of each foil is thus defined as follows:

$$C_{T,i} = -\frac{F_{x,i}}{\frac{1}{2}\rho U_\infty^2 c}. \quad (6)$$

Similarly, the power coefficient required to sustain the motion of foil  $i$  is defined as:

$$C_{P,i} = -\frac{F_{y,i}\dot{h}_i + M_{P,i}\dot{\theta}_i + F_{x,i}\dot{l}_i}{\frac{1}{2}\rho U_\infty^3 c}. \quad (7)$$

This equation is analogous to the one used by Viswanath and K. Tafti (2013), and it is derived under the hypothesis that the work required to sustain the wing motion is provided by a system moving at  $U_\infty$ . To account for the unsteady

nature of these force and power coefficients, a time-averaging operation denoted by the operator  $\overline{(\ )}$  is performed once the flow reaches a periodic behavior, typically after 3-5 cycles. This averaging is carried out over the last 4 cycles of motion. The total average coefficients considering both foils are expressed as follows:

$$\overline{C_T} = \frac{\overline{C_{T,1}} + \overline{C_{T,2}}}{2}, \quad (8)$$

$$\overline{C_P} = \frac{\overline{C_{P,1}} + \overline{C_{P,2}}}{2}. \quad (9)$$

An additional important metric is the thrust efficiency of the flapping foils, which represents the ratio between the thrust power ( $F_x U_\infty$ ) and the power required to execute the heaving, pitching and deviation motions. This efficiency is averaged over an integer number of cycles, similar to the other coefficients, and is defined for one foil as:

$$\eta_i = \frac{\overline{F_{x,i} U_\infty}}{\overline{F_{y,i} \dot{h}_i + M_{P,i} \dot{\theta}_i + F_{x,i} \dot{l}_i}} = \frac{\overline{C_T}}{\overline{C_P}}. \quad (10)$$

Since the motion of the two foils is symmetric, it is expected that  $\eta_1 = \eta_2$  most of the time. However, the resulting wake from the clap-and-fling motion may not always be symmetrical. Therefore, another average efficiency metric taking into account both foils is also considered:

$$\eta = \frac{\eta_1 + \eta_2}{2}. \quad (11)$$

The last performance metric related to the deviation motion is the instantaneous thrust coefficient standard deviation during one motion cycle. For foil  $i$ , this metric is defined as:

$$\sigma_{C_{T,i}} = \sqrt{\overline{(C_{T,i} - \overline{C_{T,i}})^2}}. \quad (12)$$

The total propulsive standard deviation which considers both foils thus yields:

$$\sigma_{C_T} = \frac{\sigma_{C_{T,1}} + \sigma_{C_{T,2}}}{2}. \quad (13)$$

This metric correlates with how leveled the thrust coefficient is, which is advisable in the case of micro air vehicles as discussed by Bos et al. (2008).

#### 2.4. Effective angle of attack

As discussed above, the flapping wing pair undergoes an effective horizontal velocity which depends on the flow velocity  $U_\infty$  and the deviation motion. As a result, modifying the deviation parameters  $\psi$  and  $l^*$  as defined in Section 2.2 affects the flow behavior directly and changes the effective angle of attack of the two foils. This necessarily impacts the performance metrics described in Section 2.3 by affecting the aerodynamic forces on the body. Based on the motion imposed and upstream flow conditions, the flapping foils pair undergoes an effective flow velocity

described as:

$$\begin{aligned}\vec{V}_{\text{eff}} &= V_x \hat{\mathbf{i}} + V_y \hat{\mathbf{j}}, \\ V_x &= U_\infty - \dot{l}, \\ V_y &= -\dot{h},\end{aligned}\tag{14}$$

With this definition, the geometrical effective angle of attack  $\alpha$  is expressed at the pivot point position as:

$$\alpha = \arctan\left(\frac{-\dot{h}}{U_\infty - \dot{l}}\right) - \theta.\tag{15}$$

On Figure 4, the effective angle of attack is thus shown to be the angle between the chord line of the foil and the effective upstream velocity vector  $\vec{V}_{\text{eff}}$ .

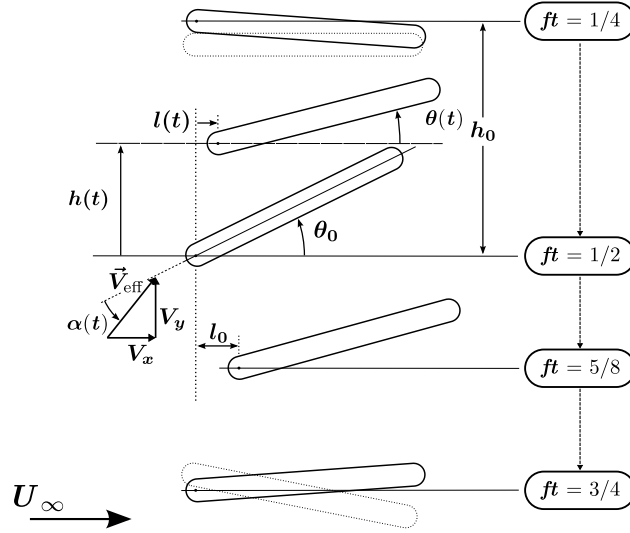


Figure 4: Imposed heaving  $h(t)$ , pitching  $\theta(t)$  and deviation  $l(t)$  motions for the upper foil ( $\phi = 105^\circ$ ,  $\psi = 0^\circ$ ). The effective velocity  $\vec{V}_{\text{eff}}$  and angle of attack  $\alpha$  are also shown.

## 2.5. Computational domain and numerical details

Figure 5 illustrates the computational domain used in this study, which consists of a  $100c \times 100c$  box. The two foils are initially positioned at a distance such that they reach the minimum spacing  $d^*$ . The boundary conditions applied are as follows: symmetry conditions are applied at the top and bottom sides of the domain, a uniform velocity inlet condition is applied on the left side, and a pressure outlet boundary condition is applied on the right side with a uniform static pressure. The flow is governed by the incompressible Navier-Stokes equations, and the numerical solutions are obtained with the commercial solver STAR-CCM+. The solver employs a second-order accurate finite-volume method that supports unstructured polyhedral overset meshes. The solution is advanced in time using a second-order backward difference scheme.

The mesh used for the simulations presented in this paper is displayed in Figure 6. It consists of a polygonal background grid (Figure 6a) with a refined central region where the two foils are located. The refined region includes two levels of refinement (Figure 6b). The first level covers the extent of the foils motion and has the same resolution as the overset meshes around the foils (Figure 6c) to ensure accurate overset interpolation. The second level, although slightly coarser, maintains a constant mesh resolution to ensure proper resolution of the near wake. The overset mesh for each foil is generated using the ICEM meshing software to have better control over the meshing process. This allows the separation of each foil's mesh into three sub-sections based on the distance from the wall. This separation protects the smaller cells of the boundary layer from being ignored by the overset interpolation when the different overset meshes come into proximity during the motion. As a result, the interpolation between each sub-section uses cells of similar size, enhancing the reliability of the results.

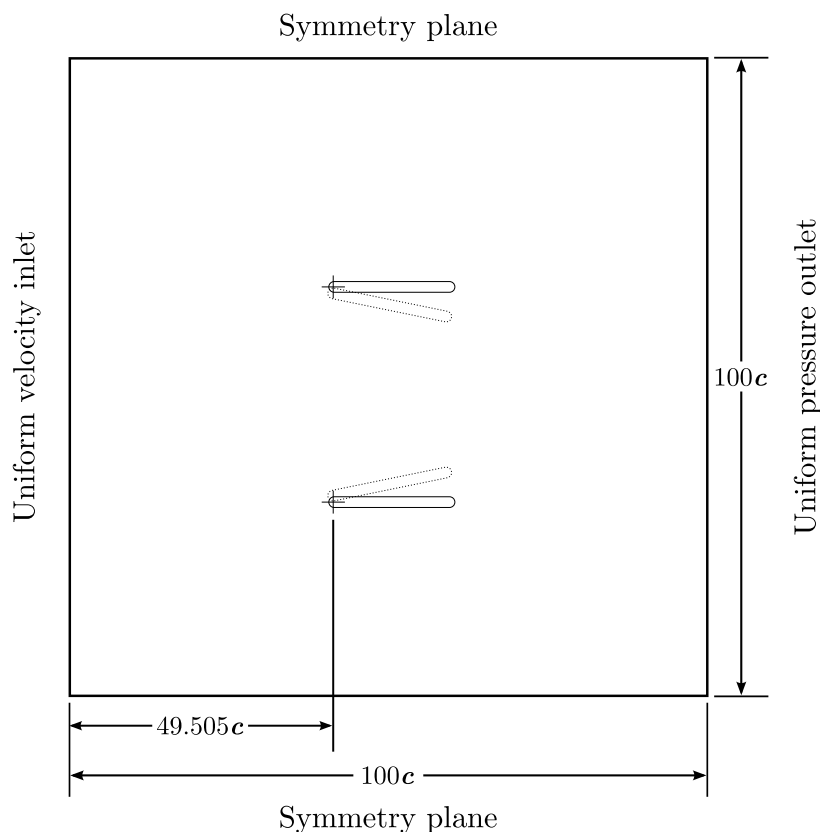


Figure 5: Computational domain of the simulation with two oscillating foils (not to scale).

### 3. Numerical verification

#### 3.1. Iterative convergence

The flow solver uses the SIMPLEC iterative algorithm to handle the pressure-velocity coupling. Therefore, appropriate stopping criteria must be met at each time step to prevent significant iterative errors. The method we used in this

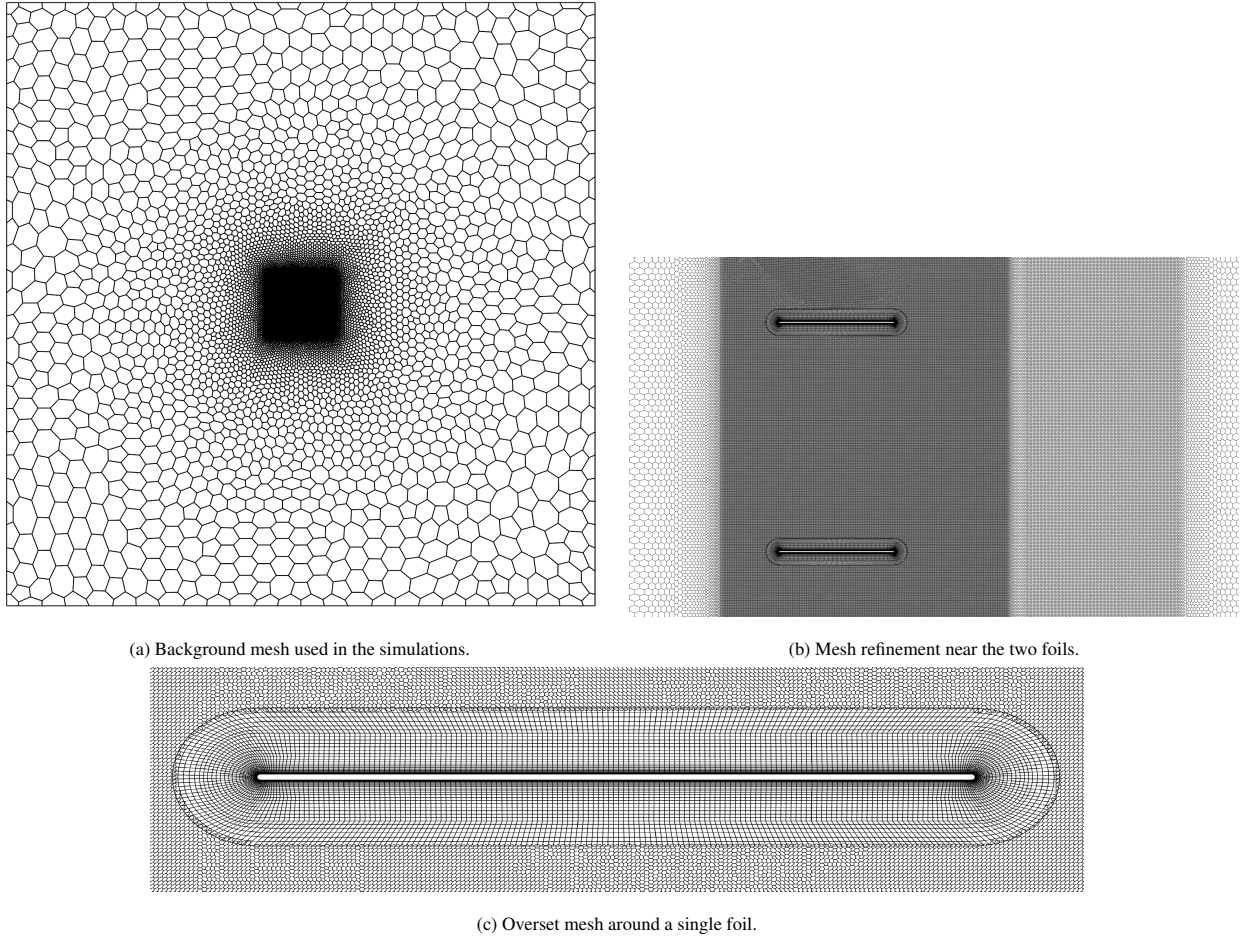


Figure 6: Baseline mesh used in the simulations.

work is an asymptotic verification on three physical quantities: the  $x$ -force, the  $y$ -force, and the moment computed on each foil (hence, there are six stopping criteria for simulations involving two foils). The asymptotic limits are normalized with five consecutive samples and are set to  $10^{-4}$ . Thus, these criteria allow direct control of the impact of the iterations on the physical quantities used for the performance evaluation. Moreover, it was verified that all equations' residuals followed a decreasing trend at each time step of the simulations, thus complementing the asymptotic limit used as the main stopping criterion.

### 3.2. Mesh and time step convergence

Three different meshes and time steps were employed to perform numerical verification and assess the discretization error. These meshes included the baseline mesh, which was used to generate the results, a coarser mesh, and a finer mesh. The number of cells for each mesh is provided in Table 2. The time step values were adjusted to ensure a consistent Courant number. The baseline dimensionless time step is  $f\Delta t = 1/2000$ .

Figure 7 illustrates the variation of the thrust coefficient during the last motion cycle for the three meshes and time steps. This particular case corresponds to a pitching phase shift of  $\phi = 105^\circ$ , a minimum spacing  $d^* = 0.005$ , a deviation amplitude  $l^* = 0.100$  and a deviation phase shift of  $\psi = 0^\circ$ . In this situation, the trailing edges of the foils approach each other closely at the end of the clap phase.

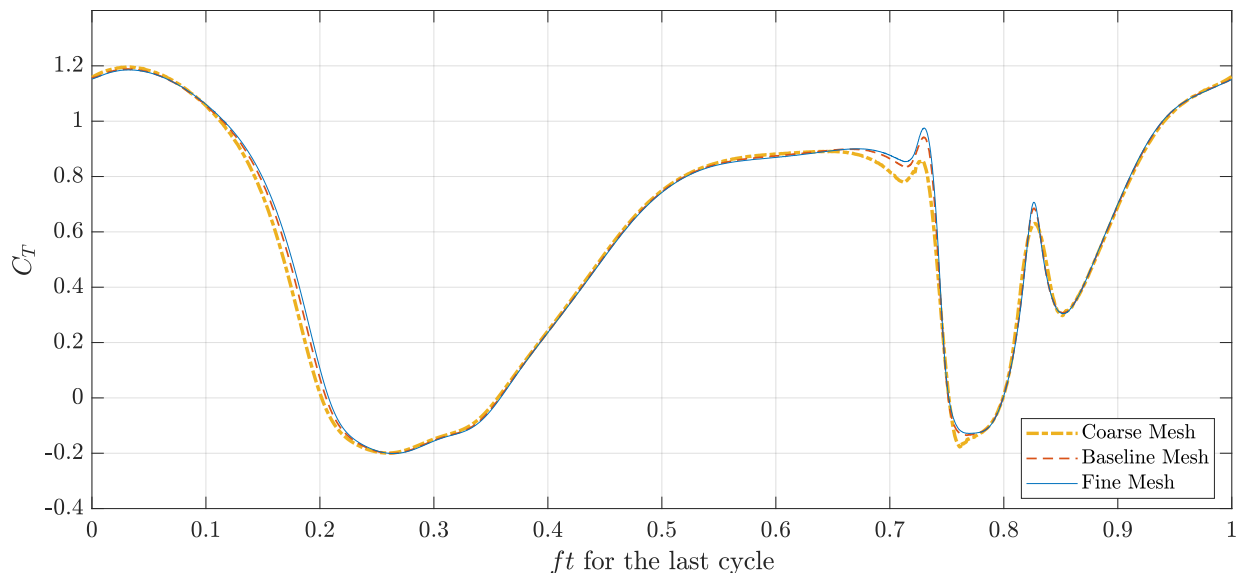


Figure 7: Convergence for the thrust coefficient for the last cycle of motion.

Upon observing Figure 7, it is evident that the curves associated with the different meshes and time steps exhibit strong similarity, indicating good convergence. However, it is also apparent that the curve corresponding to the coarser mesh displays larger discrepancies, particularly near the peaks and troughs of thrust. This behavior is expected in a converged analysis and further validates the suitability of the baseline mesh and time step. The results from Table 2 support these observations by comparing the performance metrics introduced in Section 2.3. They indicate that simultaneous spatial and temporal refinement has minimal impact on the reported physical parameters in the table, confirming the adequacy of the chosen baseline mesh and time step.

Table 2: Discretization details and cycle-averaged thrust and power coefficients.

	Total cell count	Overset zone cell count	$\Delta t \cdot f$	$\overline{C_T}$	$\overline{C_P}$
Coarse Mesh	180 199	4 140	1/1000	0.561	1.080
Baseline Mesh	672 549	11 776	1/2000	0.568	1.091
Fine Mesh	2 680 535	39 432	1/4000	0.571	1.094

Further verifications were made to assess the accuracy of the overset mesh interpolation, particularly during the time interval when the leading and trailing edges of the foils come very close. In Figure 7, two thrust peaks are observed around  $ft = 0.730$  and  $ft = 0.825$ , coinciding with substantial overlap between the overset meshes of each foil. This raises concerns regarding the number of cells in the spacing between the two foils. Indeed, a so-called hole-cutting procedure is executed by the solver during the simulation when the overset meshes overlap. This procedure activates and deactivates mesh cells depending on the proximity of the foils and their respective meshes, which can influence the mesh resolution and the quality of the mesh-to-mesh interpolation in that region. To address this concern, Table 3 presents a verification wherein local averages for the power and thrust coefficients are computed for the last cycle of each simulation within the normalized time interval  $ft \in [0.715, 0.850]$ . This interval corresponds to the two thrust peaks where the leading edges get close to each other, followed by the trailing edges that reach even closer proximity resulting from the subsequent fling of the foils. The variation in thrust and power coefficients is sufficiently low to conclude that an adequate level of convergence has been achieved, even when the foils are near and their respective meshes overlap. Based on these verifications, it can be determined that the baseline mesh with the associated normalized time step of  $\Delta t \cdot f = 1/2000$  is appropriate for the parametric study.

Table 3: Verification of the discretization in the time interval  $ft \in [0.715, 0.850]$ .

	Total cell count	Overset zone cell count	$\Delta t \cdot f$	$\overline{C_T}^1$	$\overline{C_P}^1$
Coarse Mesh	180 199	4 140	1/1000	0.276	0.545
Baseline Mesh	672 549	11 776	1/2000	0.294	0.565
Fine Mesh	2 680 535	39 432	1/4000	0.302	0.574

<sup>1</sup>  $\overline{C_T}$  and  $\overline{C_P}$  values were averaged on the normalized time interval [0.715, 0.850].

## 4. Results and discussion

### 4.1. Parametric Study Overview

In this section, the effects of varying the four parameters of interest presented in Section 2.2 are investigated. This is done according to a heuristic optimization methodology, thus by first varying the phase shift between the heaving and pitching motions as well as the minimum spacing between the airfoils without considering deviation. After identifying an optimal case by using the constant parameters defined in Equation 5 while varying the phase shift between  $60^\circ$  and  $120^\circ$  and the minimum spacing  $d^*$  between 0.005 and 8, a second parametric investigation is performed by including the deviation motion. The latter is performed by modifying the deviation amplitude  $l^*$  between 0 and 0.150, and the phase shift  $\psi$  between  $-140^\circ$  and  $40^\circ$ . While the best case identified through this heuristic

optimization may not be the absolute optimum, it remains a highly efficient configuration that yields valuable insight into the clap-and-fling mechanism.

#### Cases without deviation

The computed performances for cases without deviation based on the metrics defined in Section 2.3 are presented as a function of the phase shift for some minimum spacings between the foils, see Figure 8 and Figure 9. Similarly, computed performances for cases with deviation are presented as a function of the deviation amplitude and phase shift for both single- and dual-foils in hill charts, see Figure 12 to Figure 15.

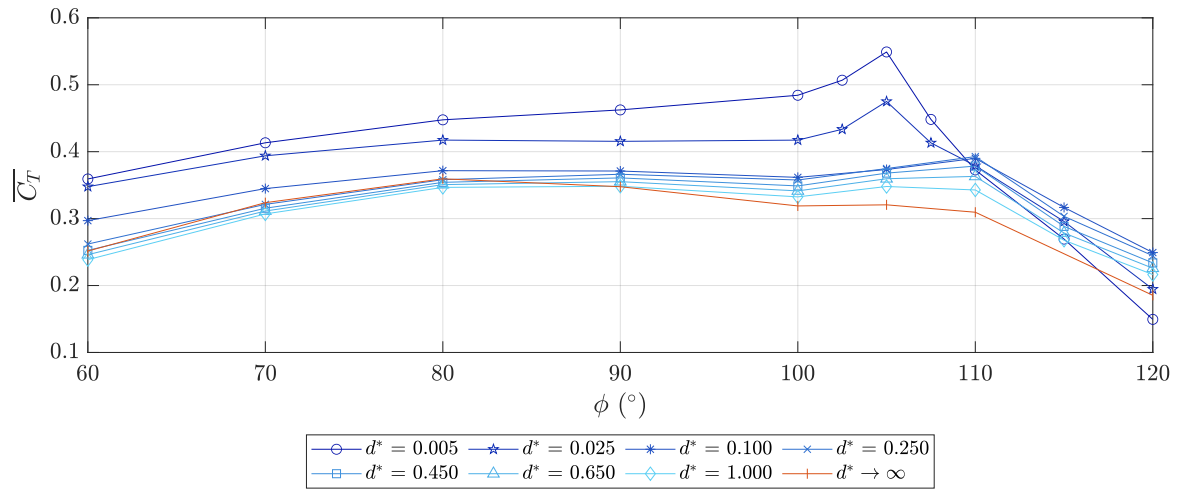


Figure 8: Averaged thrust coefficient  $\overline{C_T}$  as a function of the phase shift  $\phi$  for different minimum spacings between the foils  $d^*$  (no deviation).

Figure 8 shows that the highest thrust occurs at a phase shift of  $\phi = 105^\circ$  and a minimum spacing of  $d^* = 0.005$ . Lower and higher phase shifts result in decreased performance, while an increase in the minimum spacing between the foils results in an overall decrease in thrust for most phase shifts. At the optimal point, the averaged thrust coefficient is  $\overline{C_T} = 0.549$ . It is interesting to observe that the maximum thrust in the case of a single foil (represented here by the minimum spacing  $d^* \rightarrow \infty$ ) occurs at a different phase shift of  $80^\circ$  with a lower thrust coefficient of  $\overline{C_T} = 0.36$ . These results confirm a significant thrust improvement of up to 52.72% when using a small spacing between two flapping foils. Figure 9 shows the same trend for the efficiency: the maximum  $\eta = 0.542$  occurs at the same phase shift  $\phi = 105^\circ$  and minimum spacing  $d^* = 0.005$  for the case with two foils. Interestingly, the optimal efficiency  $\eta = 0.478$  of the single-foil case does not occur at the same phase shift as its maximum thrust, but rather at the same one as the most efficient two-foil case. Lastly, a relative efficiency increase of up to 13.50% is observed when two foils are used instead of one.

To better observe the impact of the minimum spacing between the foils, Figure 10 and Figure 11 illustrate the cycle-averaged performance metrics as a function of  $d^*$  for all the different phase shifts. As seen from Figure 10,

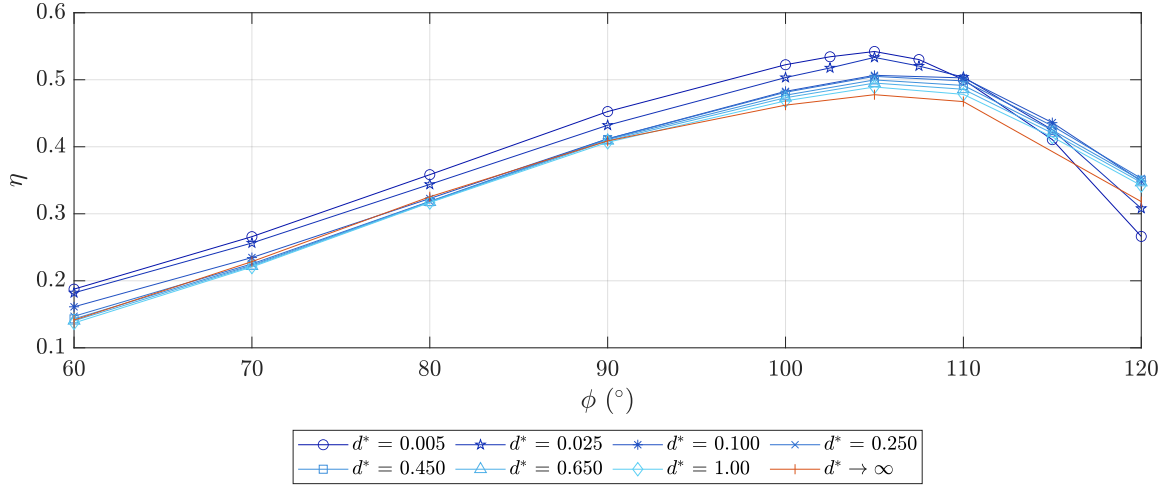


Figure 9: Efficiency  $\eta$  as a function of the phase shift  $\phi$  for different minimum spacings between the foils  $d^*$  (no deviation).

the best thrust is found at the smallest minimum spacing tested ( $d^* = 0.005$ ) and at a phase shift  $\phi = 105^\circ$ . However, as the minimum spacing increases, the curve with  $\phi = 110^\circ$  presents a higher thrust than the case with  $\phi = 105^\circ$ . In Figure 11, it can be seen that the curve associated with the phase shift  $105^\circ$  always presents the best efficiency for all of the minimum spacings  $d^*$ . At  $d^* = 1$ , the efficiency increases sharply as the minimum spacing decreases for the phase shift of  $105^\circ$  towards the lowest reported value of  $d^* = 0.005$ . This demonstrates that a near-contact minimum spacing between the foils is necessary to benefit from clap-and-fling effects. At minimum spacings of  $d^* = 8$  and above, the performances asymptotically reach those of a single foil. Concerning the best case at  $d^* = 0.005$  and  $\phi = 105^\circ$ , flow still occurs between the foils as they reach the minimum spacing. Therefore, even if the gap is relatively small, viscous

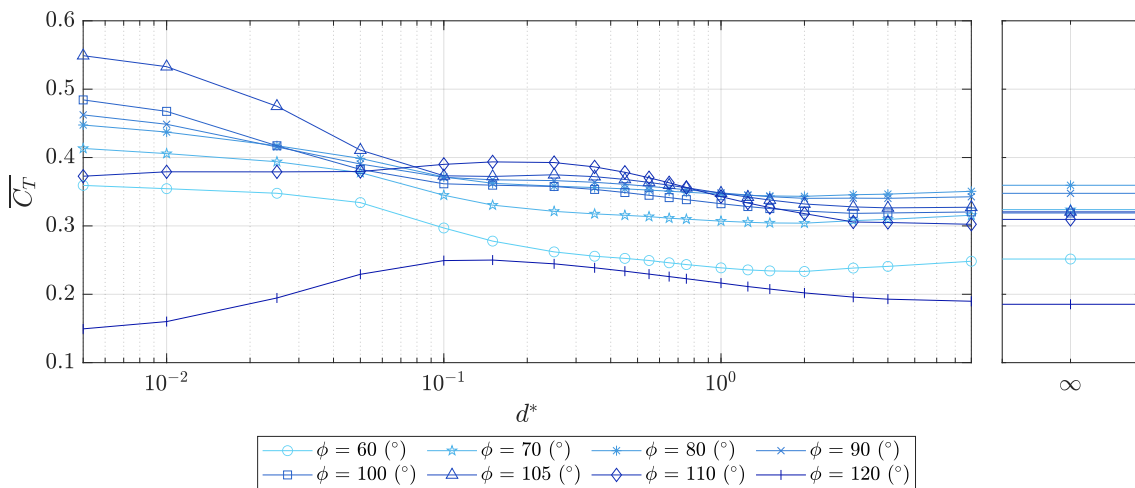


Figure 10: Averaged thrust coefficient  $\overline{C_T}$  as a function of the minimum spacing  $d^*$  for different phase shifts  $\phi$  (no deviation).

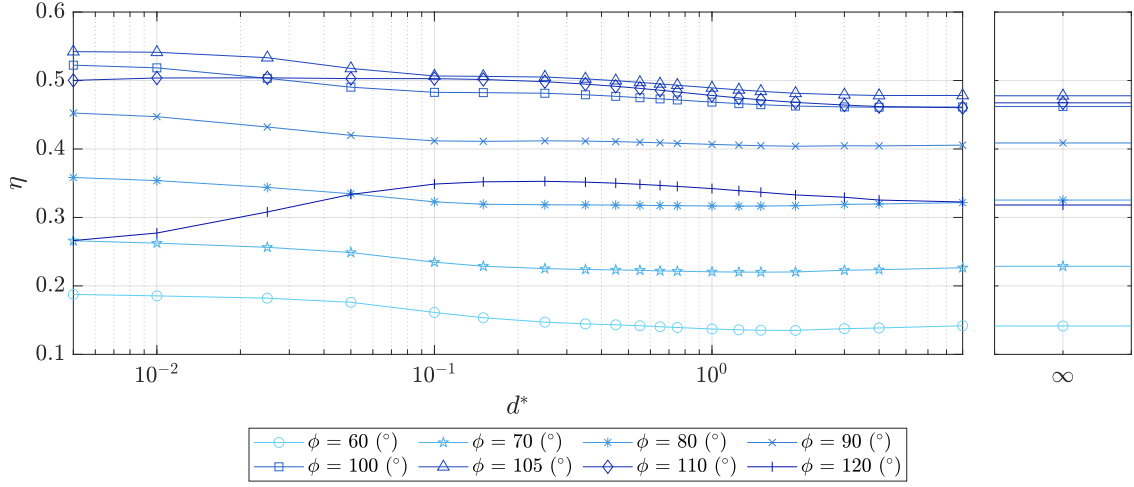


Figure 11: Efficiency  $\eta$  as a function of the minimum spacing  $d^*$  for different phase shifts  $\phi$  (no deviation).

effects in the boundary layers are not strong enough to completely block the flow between the foils. As such, the trend observed in Figure 10 and Figure 11 suggests that slight performance improvements are still possible if the minimum spacing is reduced further. However, cases with a minimum spacing smaller than  $d^* = 0.005$  were not computed in this study. Indeed, a finer mesh with prohibitive computational cost would have been necessary to accurately capture the flow within the small gap when the foils reach these minimum spacings, especially near the trailing edges.

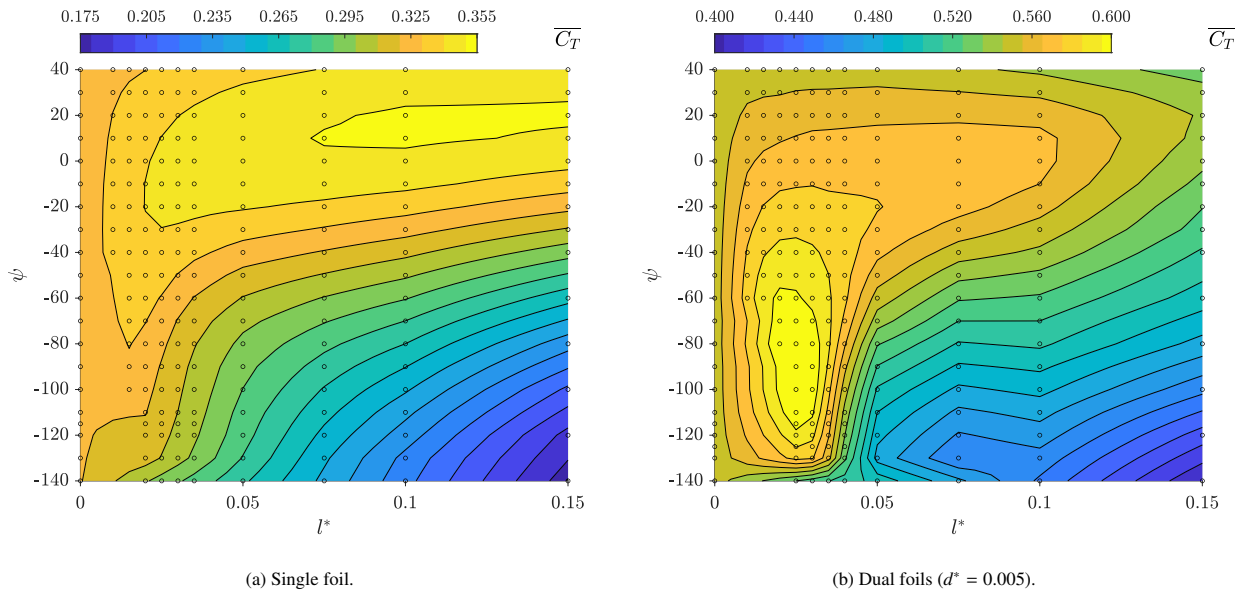


Figure 12: Averaged thrust coefficient  $\overline{C_T}$  as a function of the deviation amplitude  $l^*$  and phase shift between the deviation and heaving motions  $\psi$ .

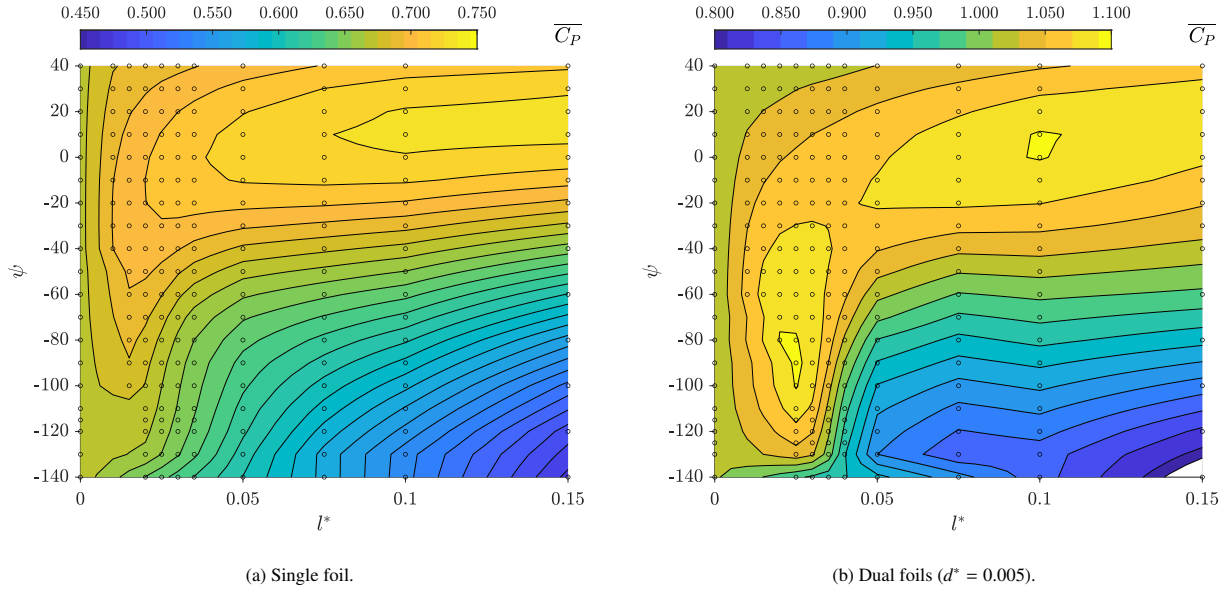


Figure 13: Averaged power coefficient  $\overline{C_P}$  as a function of the deviation amplitude  $l^*$  and phase shift between the deviation and heaving motions  $\psi$ .

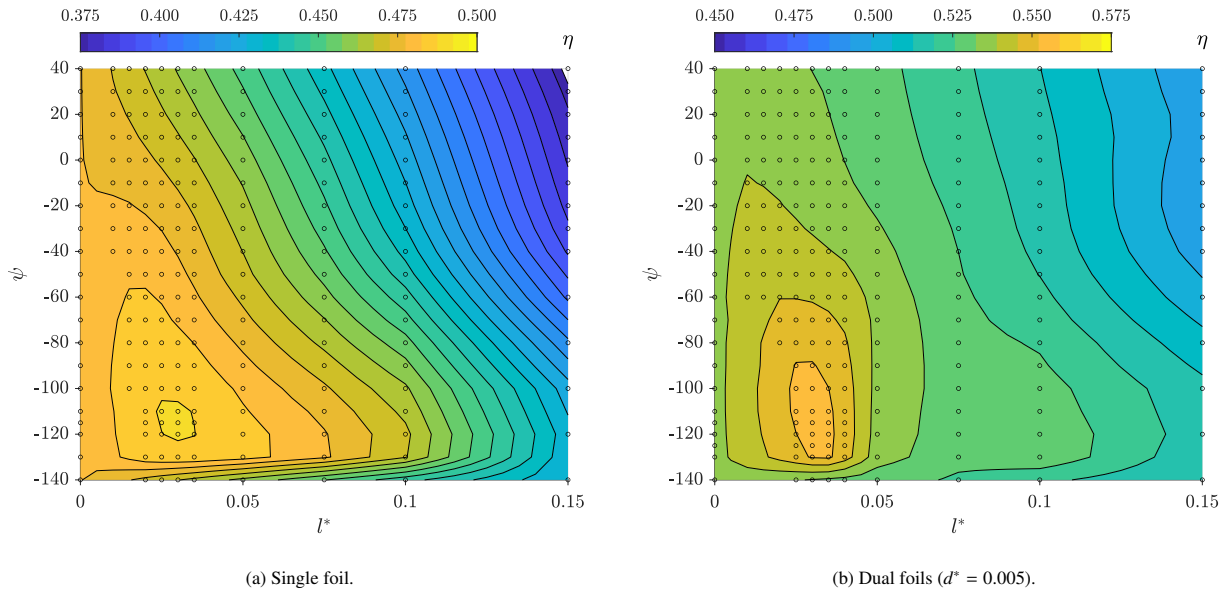


Figure 14: Efficiency  $\eta$  as a function of the deviation amplitude  $l^*$  and phase shift between the deviation and heaving motions  $\psi$ .

### Cases with deviation

Subsequently, the deviation is applied on the case with the optimal motion parameters identified above. Figure 12 shows that for a single foil, the highest averaged thrust coefficient of  $\overline{C_T} = 0.351$  occurs at a phase shift of  $\psi = 10^\circ$  and deviation amplitude  $l^* = 0.100$ . As shown on the hill chart, higher deviation amplitudes (near the maximum value considered of  $l^* = 0.150$ ) tend to increase the thrust when a positive phase shift  $\psi$  close to  $0^\circ$  is used. Interestingly,

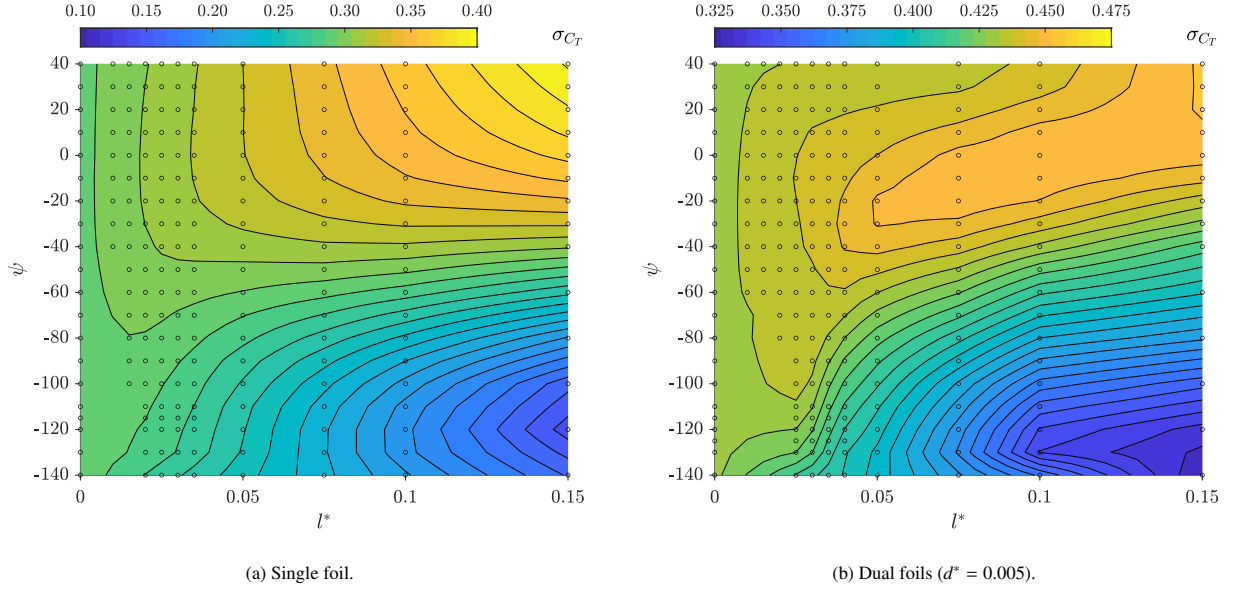


Figure 15: Propulsive standard deviation  $\sigma_{C_T}$  as a function of the deviation amplitude  $l^*$  and phase shift between the deviation and heaving motions  $\psi$ .

this is not the case for the dual foils subjected to the clap-and-fling mechanism where a lower deviation amplitude and a significant negative phase shift yield better performances. Indeed, the maximum thrust coefficient  $\overline{C_T} = 0.610$  occurs at  $\psi = -90^\circ$  and  $l^* = 0.025$ . This value represents a relative increase of 73.79% with respect to the highest reported value in single-foil cases, which is a significant improvement. As for the averaged power coefficient hill charts presented in Figure 13, similar trends to those for the thrust can be observed. Important differences are instead seen on the efficiency hill chart presented in Figure 14 where optimal efficiencies are obtained in similar regions for both single- and dual-foil cases with lower deviation amplitudes and large negative phase shifts. For the single-foil configuration, the maximum efficiency of  $\eta = 0.488$  occurs at  $\psi = -100^\circ$  and  $l^* = 0.030$  while for the dual-foil one, it occurs at  $\psi = -125^\circ$  and  $l^* = 0.035$  with a maximum value of  $\eta = 0.560$ . Thus, employing two foils yields a relative efficiency increase of up to 14.72%.

From the above discussion, we observe that using two foils subjected to clap and fling moves the optimal averaged thrust coefficient to a combination of deviation amplitude and phase shift closer to the one for the best efficiency, which is desirable. Indeed, the averaged thrust coefficient obtained at  $\psi = -125^\circ$  and  $l^* = 0.035$  is  $\overline{C_T} = 0.563$ , which represents a relative increase of 2.49% compared to the case with no deviation ( $\overline{C_T} = 0.549$ ). As for the efficiency, the value of 0.560 obtained with the same parameters represents an increase of 3.21% compared to the case without deviation ( $\eta = 0.542$ ). Therefore, properly tuning the deviation motion produces modest increases in both the thrust and efficiency in dual-foil configurations.

Moreover, it is observed in Figure 15 that increasing the deviation amplitude with negative phase shifts  $\psi$  below around  $-40^\circ$  does level the aerodynamic forces as reported by Bos et al. (2008) for both single- and dual-foil

configurations. It is also observed that the standard deviation increases with the deviation amplitude for phase shifts higher than around  $-40^\circ$ . The maximum value of the propulsive standard deviation reaches  $\sigma_{C_T} = 0.453$  for the case  $l^* = 0.150$  and  $\psi = 40^\circ$ , corresponding to a configuration with the highest deviation amplitude tested in the study. Higher values could likely be reached by increasing  $l^*$  or  $\psi$  further, but this would significantly reduce the thrust and efficiency as observed in Figure 12 and Figure 14, which is undesirable and thus not tested. For the optimal efficiency configuration of the dual-foil case, the reported value of the propulsive standard deviation is  $\sigma_{C_T} = 0.412$ . This represents a slight decrease compared to the base case without deviation where  $\sigma_{C_T} = 0.429$ . Therefore, in addition to increasing efficiency, a negative phase shift of  $\psi = -125^\circ$  at a deviation amplitude of  $l^* = 0.035$  also slightly levels the unsteady forces resulting from the whole flapping motion. On the other hand, the dual-foil configuration producing the best thrust ( $C_T = 0.610$  with  $\psi = -90^\circ$  and  $l^* = 0.025$ ) presents a slightly higher propulsive standard deviation of  $\sigma_{C_T} = 0.436$ , corresponding to more force variations throughout a motion cycle compared to the case without deviation. Section 4.2 and Section 4.4 further discuss these aspects by analyzing the flow field topology against the kinematics of the flapping foils using the deviation motion.

## 4.2. Flow fields topology

### *Cases without deviation*

Figure 16 shows the vorticity field of the best case without deviation for thrust and efficiency ( $d^* = 0.005$  and  $\phi = 105^\circ$ ) at several time frames during one motion cycle. As seen in the figure, flow separation occurs during the clap motion on the boundary layers of each foil along with the formation of leading-edge vortices. However, because of the low reduced frequency ( $f^* = 0.15$ ), each vortex shed from the leading edge is convected quickly in the wake, which minimizes its interaction with the foils. This wake behavior is thus in agreement with that of a single foil as shown by Olivier (2014).

In addition, the best thrust and efficiency configurations exhibit moderate leading-edge vortices. Such vortices in low-Reynolds-number flow regimes are known to modulate significantly aerodynamic forces because of the low-pressure zone within their core. In addition, even though the flow separates near the leading edges to form vortices, it may remain attached at the trailing edges, maintaining a smooth flow that satisfies the Kutta condition (Sane, 2003). This phenomenon is known as delayed stall, and it strongly depends on the motion parameters in flapping foils (Chen et al., 2020). In the current study, the optimal phase shift of  $\phi = 105^\circ$  combined with the reduced frequency  $f^* = 0.15$  and baseline pitching amplitude  $\theta_0 = 30^\circ$  allows the foils to change their course before actual stall occurs. In the meantime, the foils benefit from high thrust because of their high angle of attack.

Furthermore, it is observed in Figure 16 that the minimum spacing occurs at the trailing edge during the motion. This is a key aspect of the clap-and-fling mechanism since the flow between the two foils is mainly responsible for generating thrust improvements. Indeed, when the minimum spacing is reached at the trailing edge at  $ft = 0.85$ , the fluid between the foils is ejected downstream at high speed. This build-up of high velocity can be better observed in Figure 17, which presents the instantaneous velocity vector field. As stated by Shyy et al. (2007), this fast flow

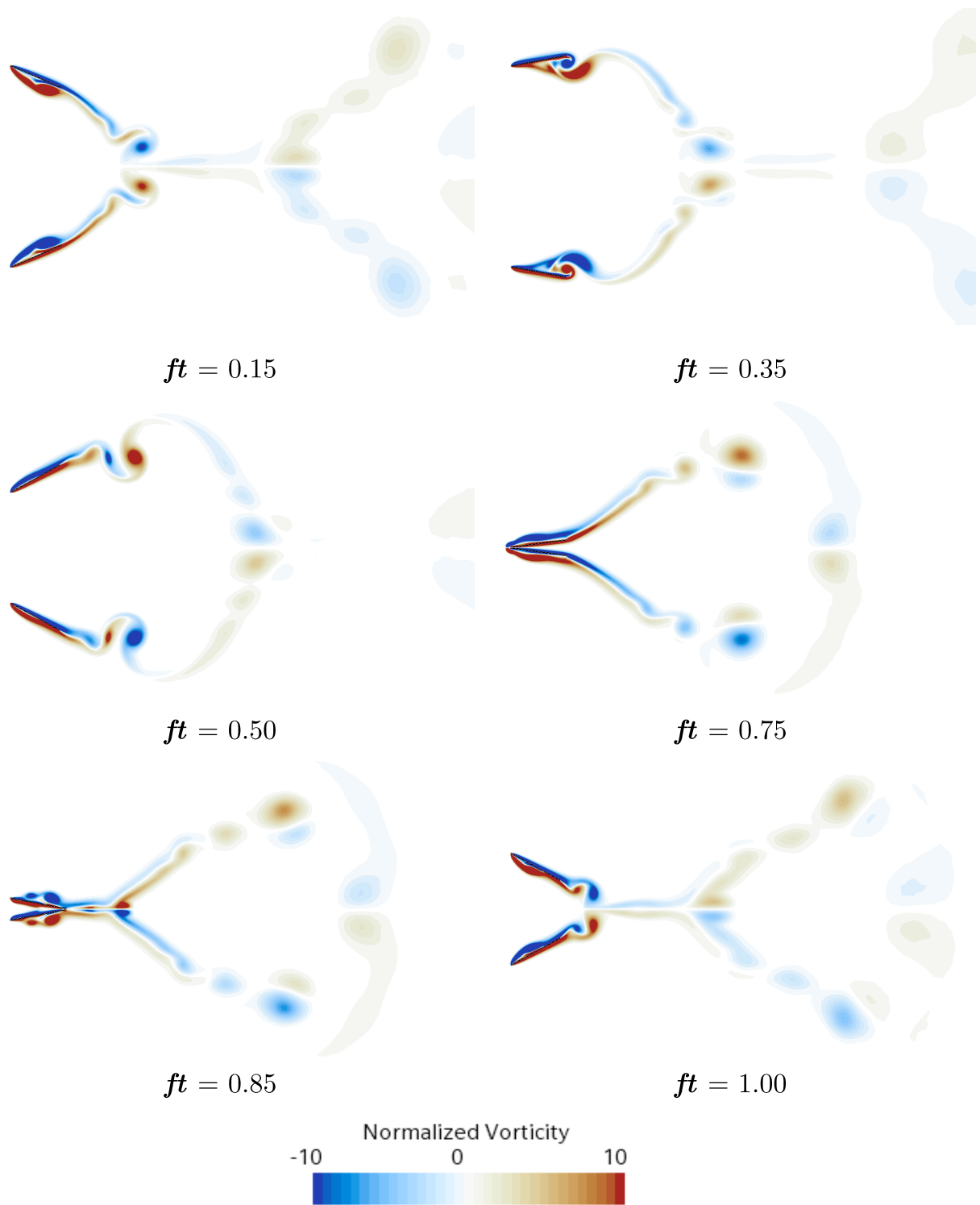


Figure 16: Normalized vorticity field ( $\omega c/U_\infty$ ) for  $\phi = 105^\circ$  and  $d^* = 0.005$ .

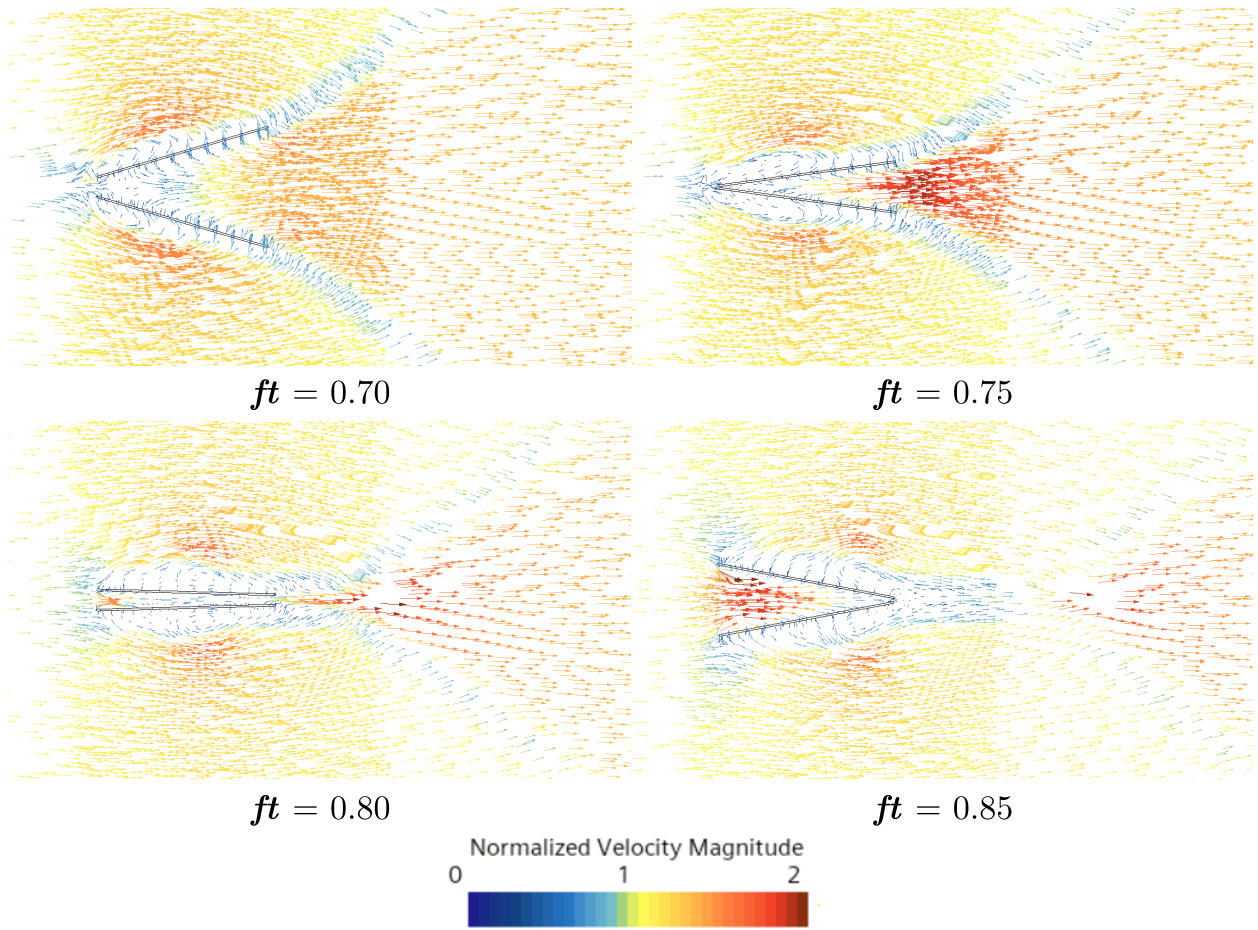


Figure 17: Velocity vector field for  $\phi = 105^\circ$  and  $d^* = 0.005$ . The vector length is scaled with the normalized velocity magnitude.

ejection allows the trailing edge vortex of each wing to be shed more quickly in the wake, which mitigates the Wagner effect where a latency typically occurs in the establishment of circulation of the foils' bound vortices counteracted by the trailing edge vortices. As a result, the thrust generation resulting from this quick circulation buildup is greatly accelerated. As for the subsequent fling phase, fluid is inhaled upstream of the foils into the gap created as they separate, greatly increasing circulation. This causes strong vortex generation at their leading edges on the inner surfaces, as seen at  $ft = 1.00$  in Figure 16. This fast circulation of opposite signs buildup on each foil generates high thrust on the two foils. This mechanism is analogous to a ground effect observed in various aerodynamics applications.

In the case of flapping wings undergoing clap and fling, a ground-effect-like phenomenon occurs when the foils reach proximity during the clap phase. This is shown in Figure 18 and Figure 19 where a comparison of the normalized pressure field and velocity vector field for the best dual-foil case with  $\phi = 105^\circ$  and  $d^* = 0.005$  with the equivalent single-foil case is presented at  $ft = 0.826$  (when the minimum spacing is reached at the trailing edge). The presence of the second foil produces a symmetry where streamlines are deviated so that they are parallel to the symmetry plane. Indeed, this symmetry is similar to that of a solid boundary if we neglect viscous effects and thus confine the flow

between the two foils, changing its behavior. This is observed in the velocity vector field where the fluid begins to accelerate between the foils as they start to separate during the fling phase of the motion. Through the latter and with the inclination of the foils, a ground effect occurs and greatly diminishes the already present low-pressure zone observed on the lower surface of the single foil. Therefore, the force distributions are affected, which predominantly increases the thrust.

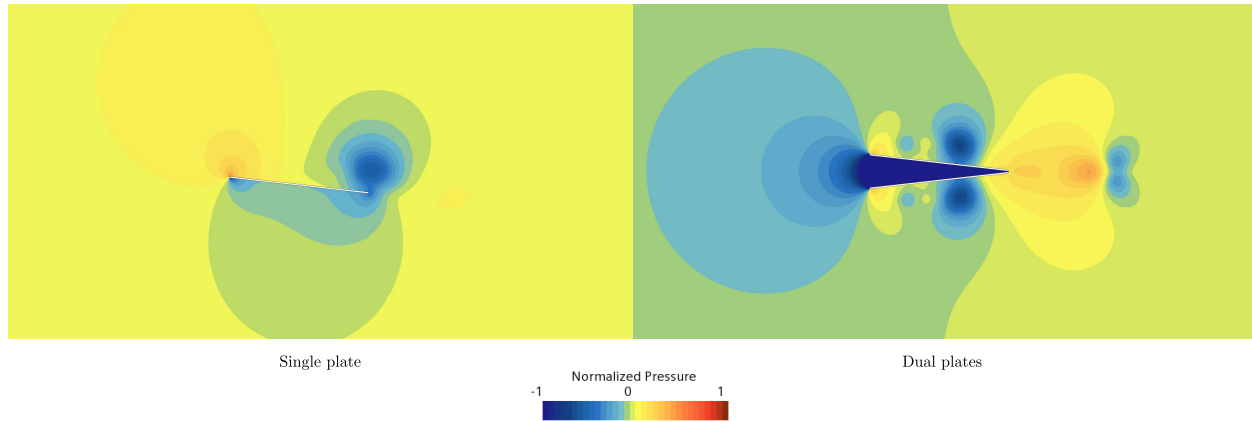


Figure 18: Comparison of the normalized pressure field ( $p/(\rho U_\infty^2)$ ) of the single- and dual-foils cases with  $\phi = 105^\circ$  and  $d^* = 0.005$  at  $ft = 0.826$ .

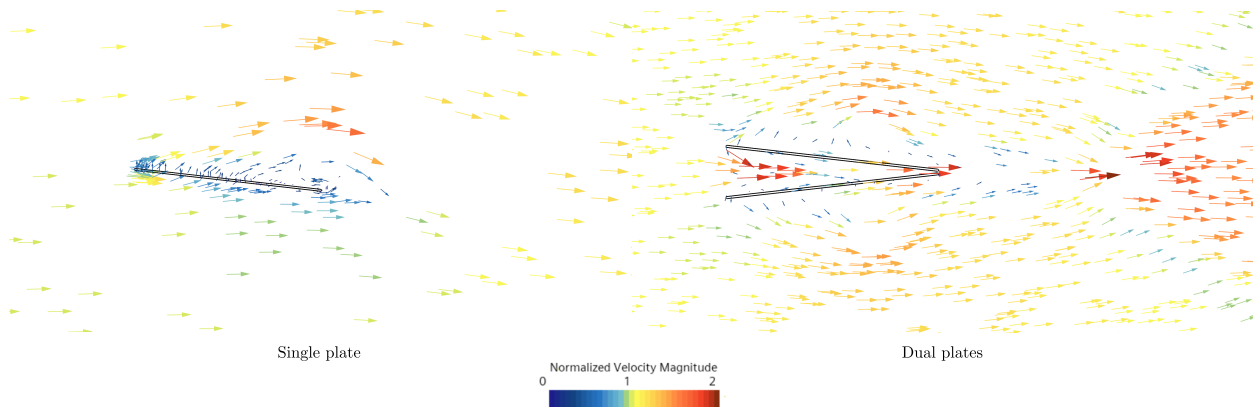


Figure 19: Comparison of the velocity vector field for the single- and dual-foil configurations with  $\phi = 105^\circ$  and  $d^* = 0.005$  at  $ft = 0.826$ . The vector length is scaled with the normalized velocity magnitude.

To better understand the impact of the kinematics on the clap-and-fling performance improvement, vorticity and velocity fields of another case are presented in Figure 20 and Figure 21. It can be seen that the change in phase shift significantly impacts the kinematics of the foils as the minimum spacing occurs at the leading edge at  $ft = 0.75$  for this case. This configuration blocks the fluid upstream of the foils from being injected in between and thus reduces its thrust and efficiency. Since the minimum spacing now occurs at the leading edge, the boundary layers detach around  $ft = 0.85$  when the spacing increases. The fluid is then convected downstream at a lower velocity when compared to the optimal case. Indeed, Figure 21 also shows high-velocity vectors upstream of the foils near their leading edges

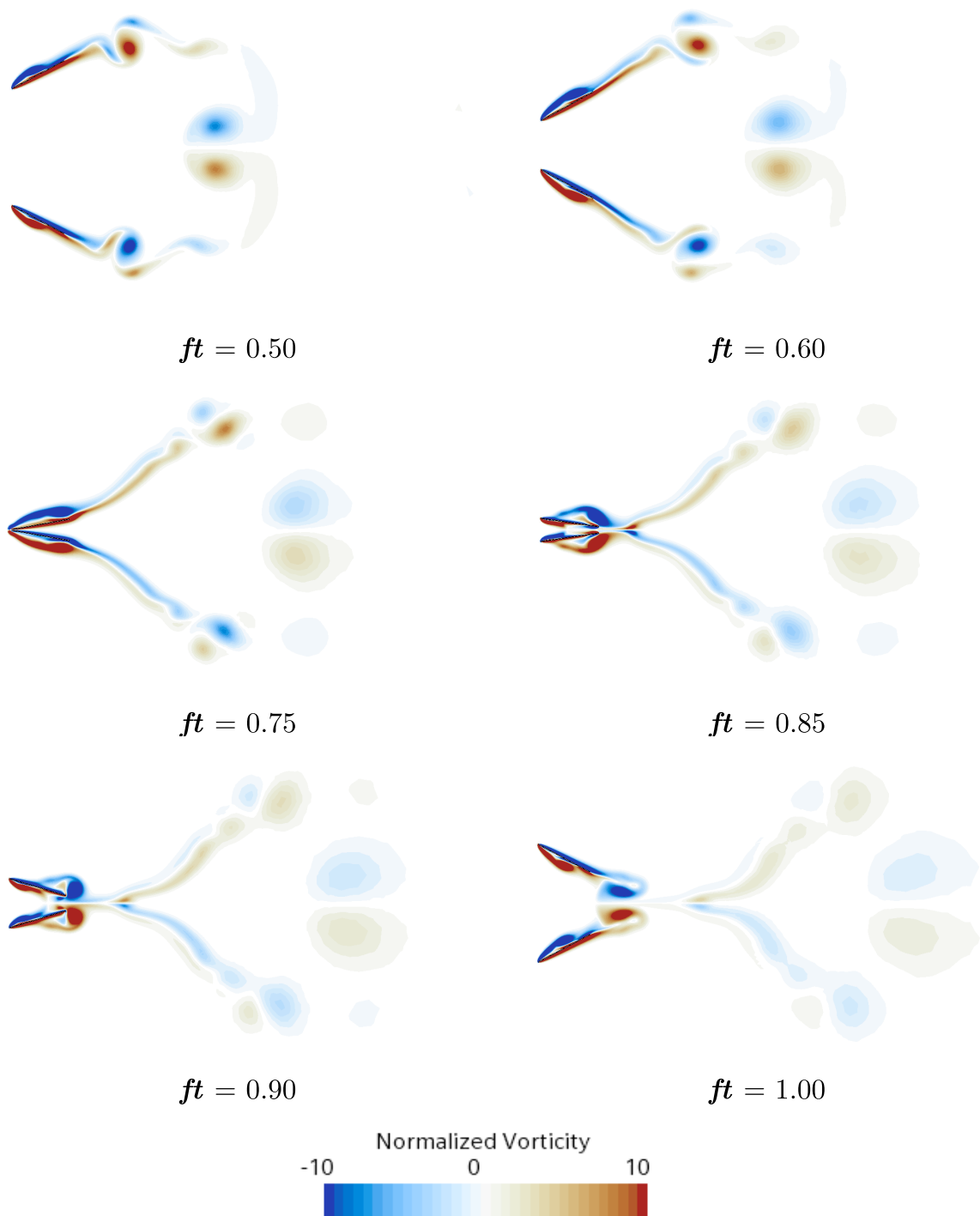


Figure 20: Normalized vorticity field ( $\omega c/U_\infty$ ) for  $\phi = 110^\circ$  and  $d^* = 0.005$ .

during the clap phase, which is detrimental to the thrust. The latter is thus consequently lower, and the trailing edge vortices of each wing are convected more slowly. These observations emphasize the importance of the phase shift,

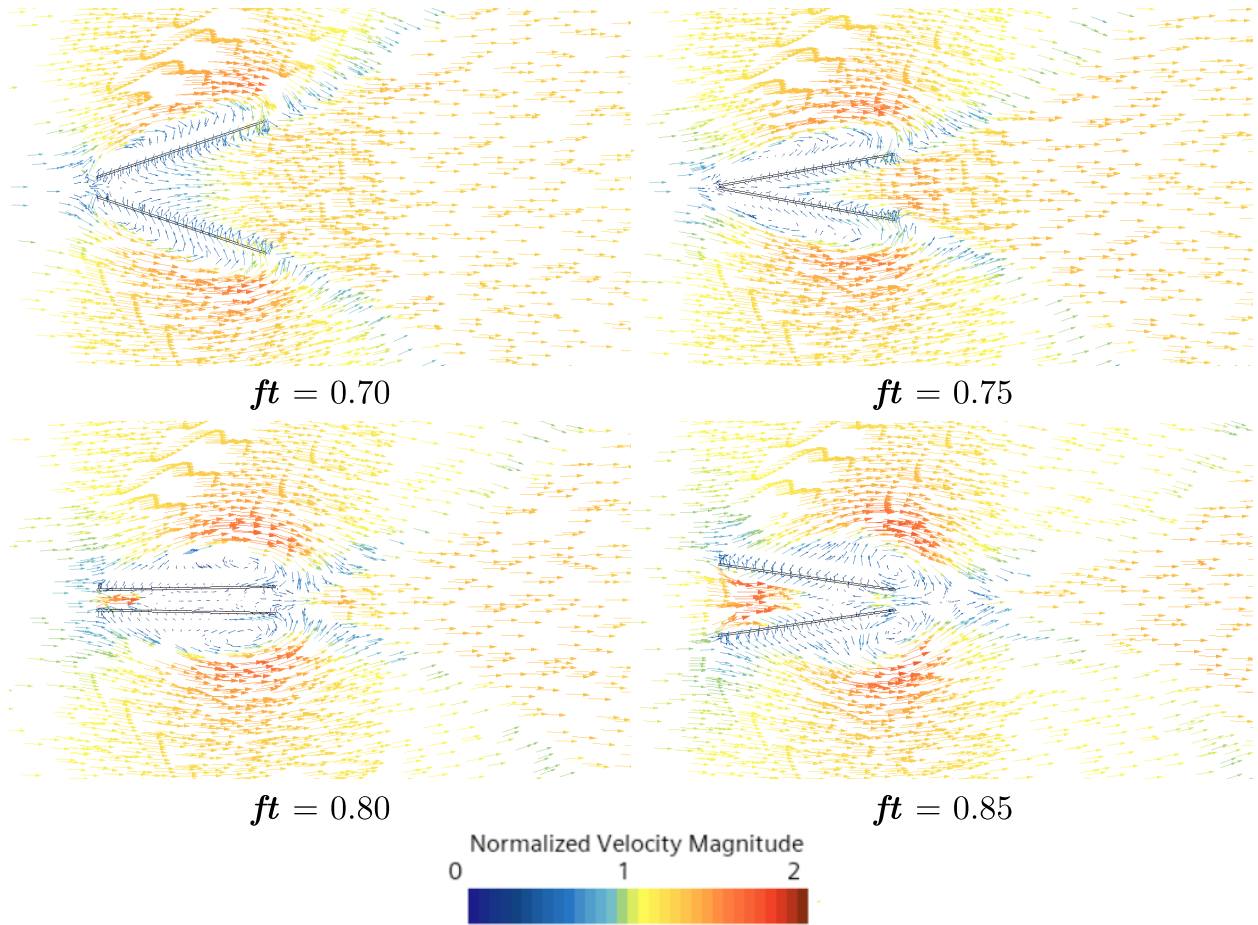


Figure 21: Velocity vector field for  $\phi = 110^\circ$  and  $d^* = 0.005$ . The vector length is scaled with the normalized velocity magnitude.

particularly at small minimum spacings. If not properly chosen, the flow can be stuck between the foils, resulting in suboptimal thrust performances. A phase shift of  $\phi = 105^\circ$ , which is higher than the typical case of  $\phi = 90^\circ$ , is necessary to increase the performances. However, phase shifts larger than  $105^\circ$  impede the flow by changing the chordwise position of the minimum spacing between the foils.

To support this discussion further, static pressure contours for the two previous cases are presented respectively in Figure 22 and Figure 23. For the optimal case with  $\phi = 105^\circ$ , it can be seen in Figure 22 that a high positive static pressure zone is present to the right (downstream) of the foils during the clap phase, which tends to push the foils to the left and thus contribute to the thrust. As the foils move closer to each other, this positive pressure only increases with a negative pressure zone building to the left of the foils as their inclination changes. As the foils undergo the clap-and-fling motion, this low-pressure zone only gets larger in size and magnitude thus pushing once again the foils in the direction opposite to the flow.

For the case with  $\phi = 110^\circ$  presented in Figure 23, the positive pressure zone during the clap phase is not as high in magnitude and thus results in a lower thrust. Moreover, low pressure develops between the foils after they

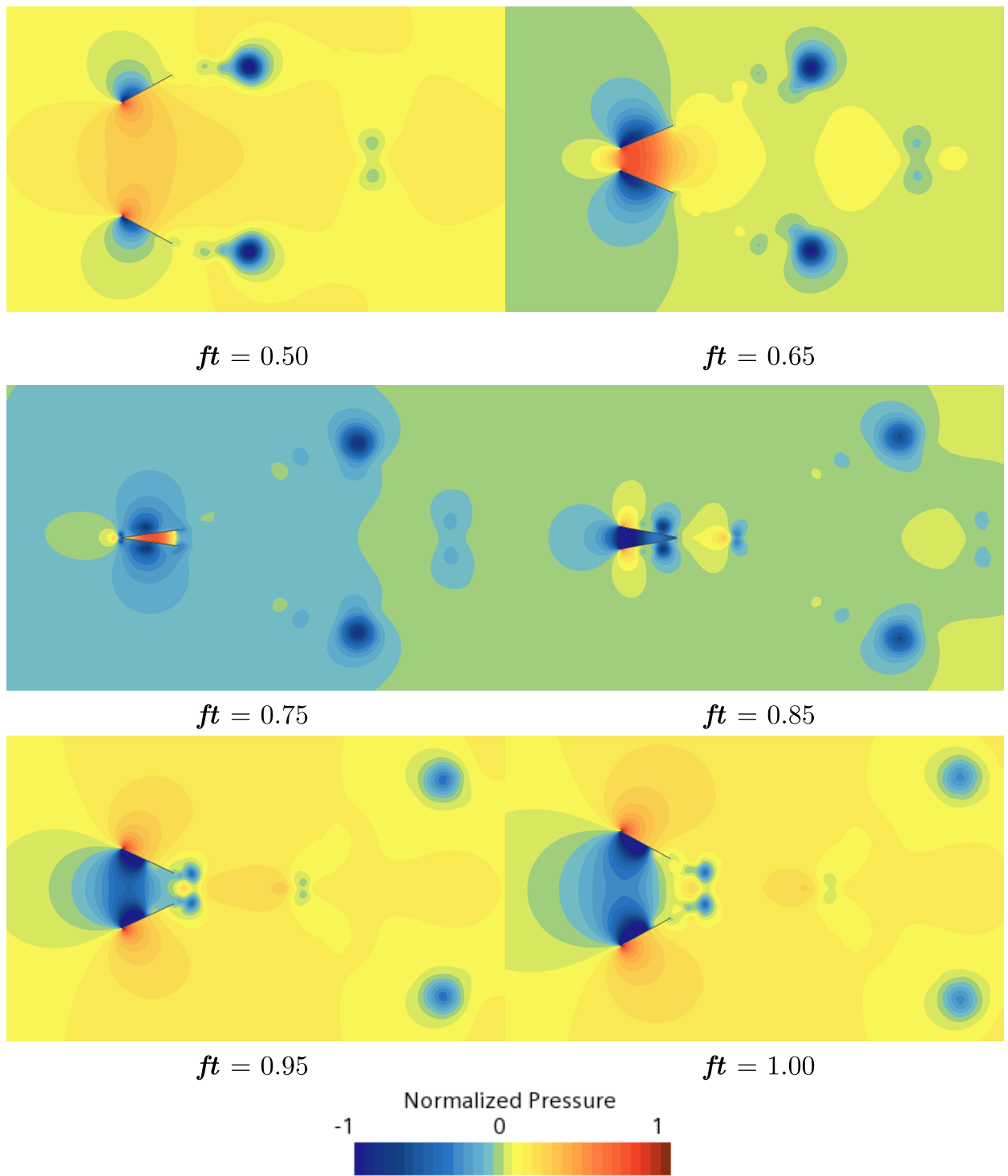


Figure 22: Normalized pressure field ( $p/(\rho U_\infty^2)$ ) for  $\phi = 105^\circ$  and  $d^* = 0.005$ .

reach their minimum spacing at the leading edge. At the same time, the vortex core on the outer side of each foil produces a low-pressure zone near the trailing edge (see Figure 20 between time  $ft = 0.85 - 1.00$ ). The resulting

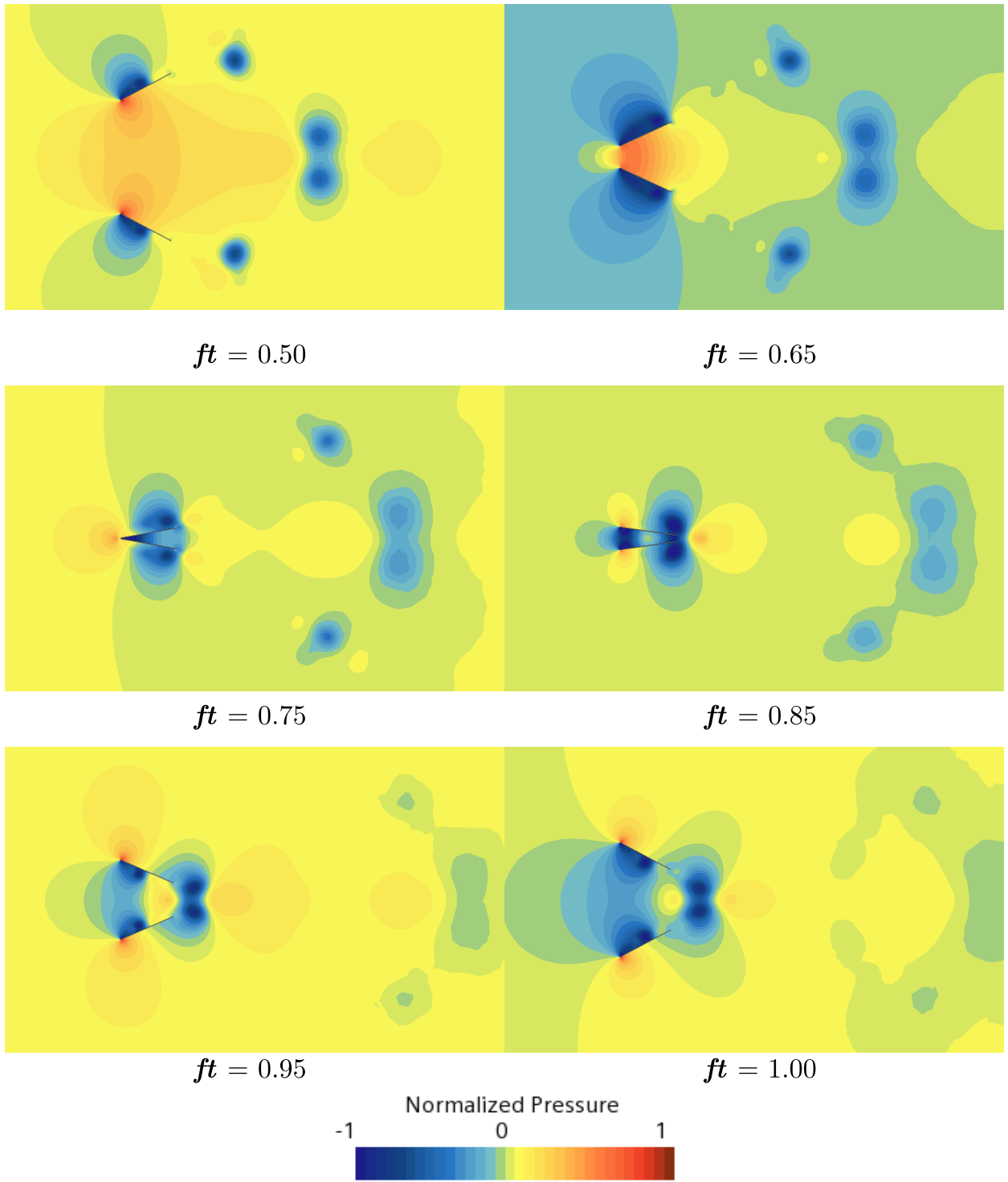


Figure 23: Normalized pressure field ( $p/(\rho U_\infty^2)$ ) for  $\phi = 110^\circ$  and  $d^* = 0.005$ .

pressure gradient between these two low-pressure zones is thus very small, which produces low instantaneous thrust subsequently. Additionally, the closing gap at the leading edge at  $ft = 0.75$  produces a stagnation effect that increases the pressure at this location, producing a local force that counteracts the thrust.

#### *Cases with deviation*

Including the deviation motion has effects on the flow field to some extent. Firstly, the pressure and vorticity fields of several cases of interest based on the results discussed in Section 4.1 are presented. These fields are shown at  $ft = 0.85$ , which was identified in Section 4 as a key instant where the trailing edges of the foils reach the minimum spacing  $d^*$  and generate a significant thrust peak. The basis of comparison is the configuration with no deviation ( $l^* = 0, \psi = 0^\circ$ ) and is first compared to the case including deviation with the best efficiency ( $l^* = 0.035, \psi = -125^\circ$ ). Since this deviation amplitude is moderate, there are no significant differences between the two cases in the flow fields during one period of motion, which agrees with similar results by Jung et al. (2024). The performance improvements will thus be explained by a different approach in Section 4.4. The last case of interest with  $l_0 = 0.150$  and  $\psi = 40^\circ$  represents a configuration with substantial deviation where the propulsive standard deviation  $\sigma_{C_T} = 0.453$  is the highest in the range of  $l^*$  considered in this parametric study. For such a configuration, important differences are noticeable in the flow fields. Indeed, Figure 24 shows that this case exhibits important flow separation on both flapping foils and more leading-edge vortices. These are eventually shed in the wake as shown in Figure 24 where the strongest visible vortices are being ejected near the trailing edges of the foils.

Leading-edge vortices are known to modulate significantly aerodynamic performances due to the low-pressure zone contained within their core (Sane, 2003; Chen et al., 2023). In the cases with no deviation ( $l^* = 0$ ) and moderate deviation ( $l^* = 0.035, \psi = -125^\circ$ ), these leading-edge vortices are moderate and are formed with proper timing, producing high thrust. In the case with significant deviation ( $l^* = 0.150, \psi = 40^\circ$ ), flow separation and generation of several leading-edge vortices prevent the flow from remaining attached at the trailing edges, causing stall to occur. This is most noticeable when the foils are close to each other at their trailing edges around the instant  $ft = 0.85$ , as shown in Figure 24. The stronger leading-edge vortices generated in this case create an important low-pressure zone downstream of the foils as observed in Figure 25, which counteracts the other favorable low-pressure zone upstream of the foils produced by the clap-and-fling motion. This significantly reduces thrust and demonstrates that configurations with large deviation may severely impair the evolution of the flow and decrease the overall performance while increasing propulsive standard deviation  $\sigma_{C_T}$  if the deviation parameters are not properly chosen.

#### *4.3. Instantaneous effects on force and power coefficients*

So far, the best cases of thrust and efficiency have been established against the minimum spacing between the foils  $d^*$  and the phase shift  $\phi$ . However, Figure 10 and Figure 11 introduced earlier also present the thrust coefficient and efficiency of single-foil cases, which correspond to the points labeled with  $d^* \rightarrow \infty$ . As defined in Section 2.3, the thrust and power coefficients for the dual-foil simulations are averaged according to Equation 8 and Equation 9 to

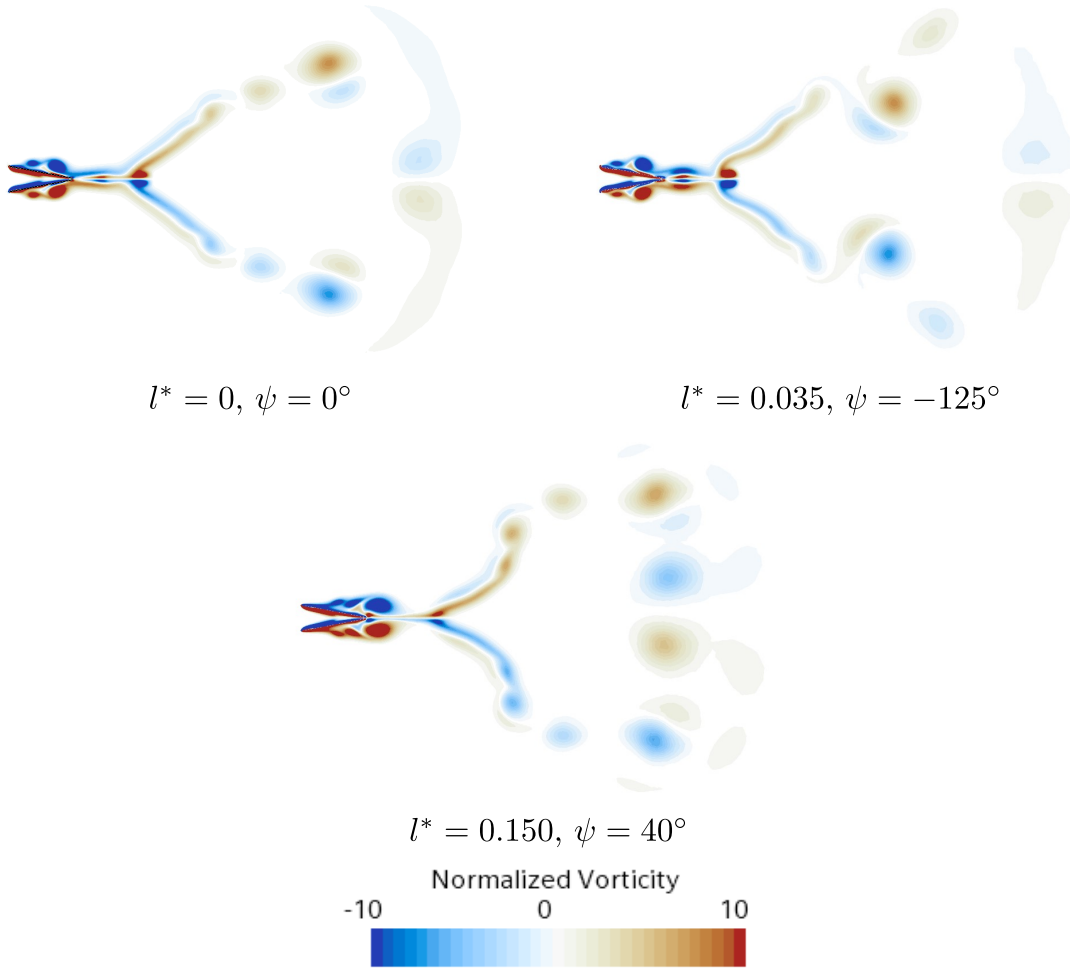


Figure 24: Normalized vorticity field ( $\omega c/U_\infty$ ) of the two foils for different combinations of  $\psi$  and  $l^*$  at  $ft = 0.85$ .

obtain an equivalent performance metric to a single-foil case. As seen in these figures, the curves for each phase shift reach an asymptote as  $d^*$  increases towards the case of the single foil. Indeed, the thrust coefficient and efficiency are almost identical at  $d^* = 8$  and  $d^* \rightarrow \infty$ , which provides a valuable indication of the distance required to produce significant clap-and-fling effects.

Plots of the instantaneous thrust and power coefficient during one cycle are now compared to assess the performance improvements obtained by using two foils subjected to the clap-and-fling phenomenon. As seen in Figure 26 and Figure 27, using two foils generally increases both the required power and the thrust. For the dual-foil simulations, the maximum power and thrust obtained during the downstroke and the upstroke of a given foil are indeed different. Figure 27 shows this maximum thrust of  $C_T = 0.75$  at  $ft = 0.08$  for the single-foil case and  $C_T = 1.25$  at  $ft = 0.078$  for the best dual-foil case. These thrust peaks are caused by the foils' acceleration and occur during the upstroke of the foils after the stroke reversal performed during the clap phase of the previous motion cycle. Indeed, at

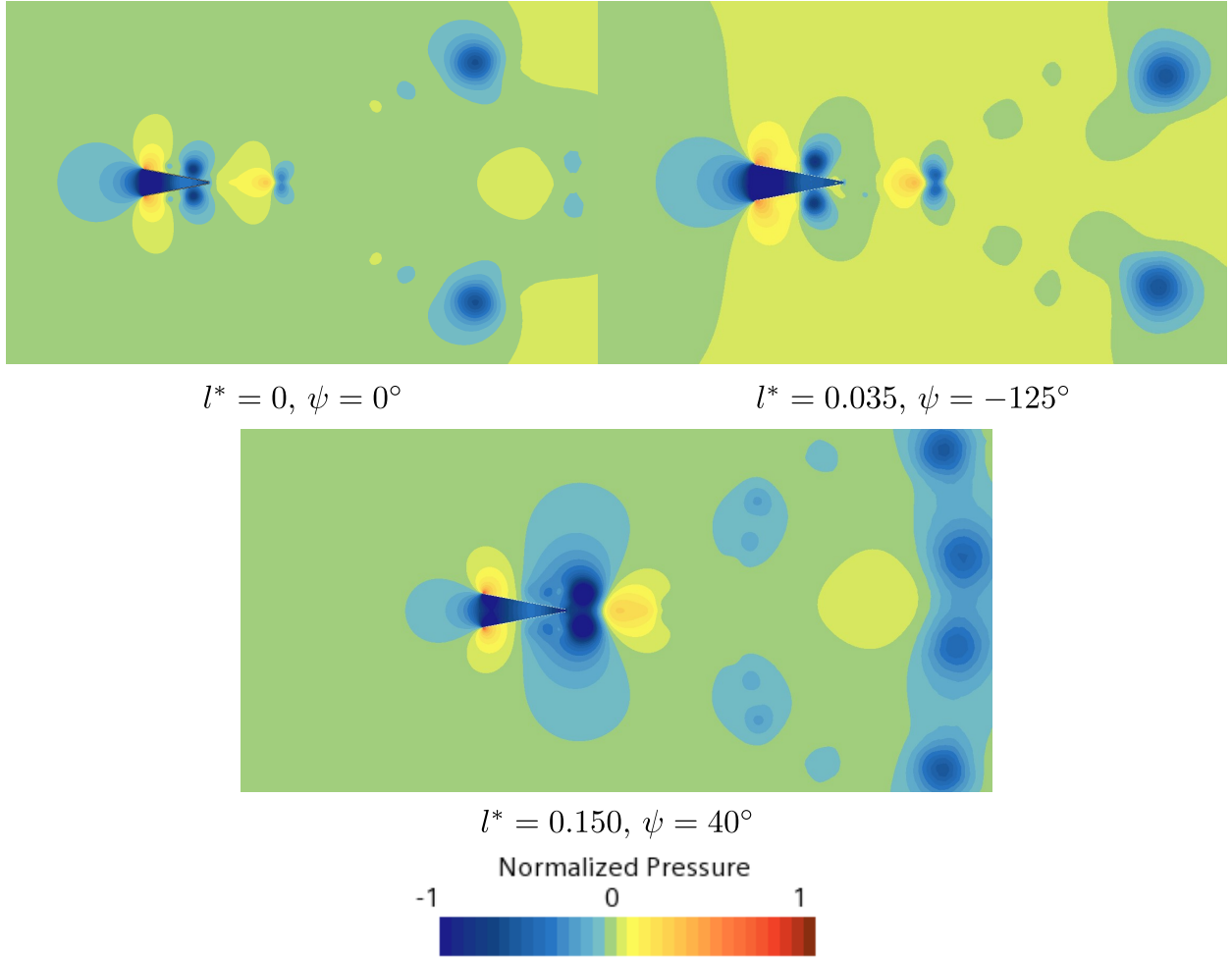


Figure 25: Normalized pressure field ( $p/(\rho U_\infty^2)$ ) of the two foils for different combinations of  $\psi$  and  $l^*$  at  $ft = 0.85$ .

these specific times in the cycle, strong vorticity layers are produced in a short amount of time. This results in a large rate of change of fluid impulse and, in turn, increases the thrust (Sun and Tang, 2002).

After the second stroke reversal of the foils observed around  $ft = 0.30$ , several other thrust peaks are observed in Figure 27. The most expected one has a thrust coefficient of  $C_T = 0.78$  and occurs at  $ft = 0.826$  as the foils get close to each other while the fluid is quickly convected downstream in the wake. This corresponds to when the foils reach their minimum spacing  $d^*$  at the trailing edge. At the same time, the required power also peaks at  $C_P = 1.01$ . Moreover, an interesting observation is a local peak of power and thrust observed during the clap phase near  $ft = 0.729$ . This corresponds to the instant where the leading edges of the foils are at their closest distance to each other, with a large positive pressure zone between them immediately to the right of the leading edges. The instantaneous performance metrics obtained at this peak are  $C_P = 1.38$  and  $C_T = 1.02$ . Interestingly, this instant represents the second-highest thrust peak encountered during the motion while the power does not increase as much. Thus, this results in an overall increase in the instantaneous contribution to efficiency which, in turn, improves the

cycle-averaged performance metrics and highlights the benefits of moving the foils close to each other during their motion. As mentioned, a proper phase shift ensures the minimum spacing  $d^*$  between the foils is located at their trailing edges.

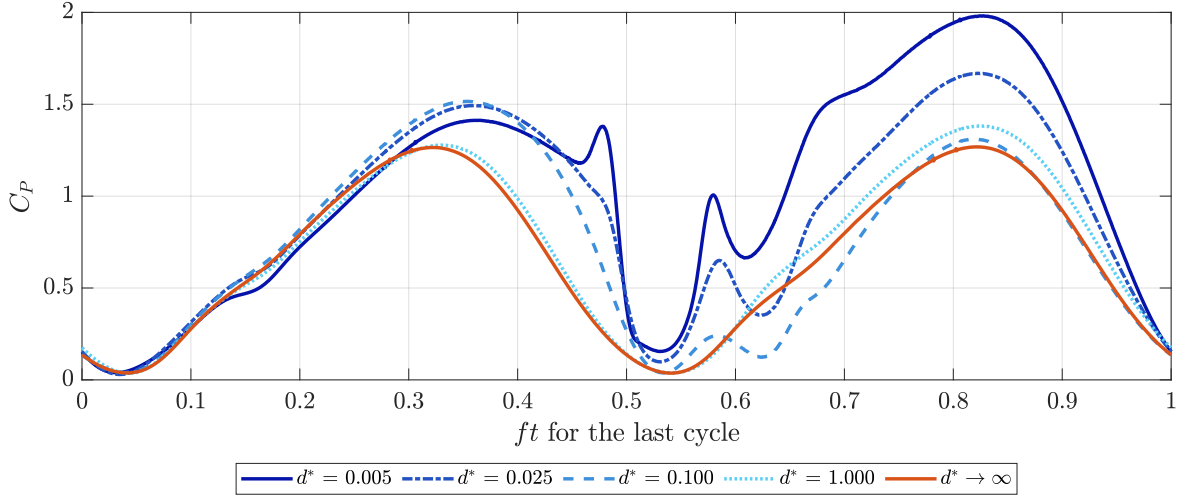


Figure 26: Comparison of the power coefficient  $C_P$  for  $\phi = 105^\circ$  between the single-foil case and several dual-foil cases.

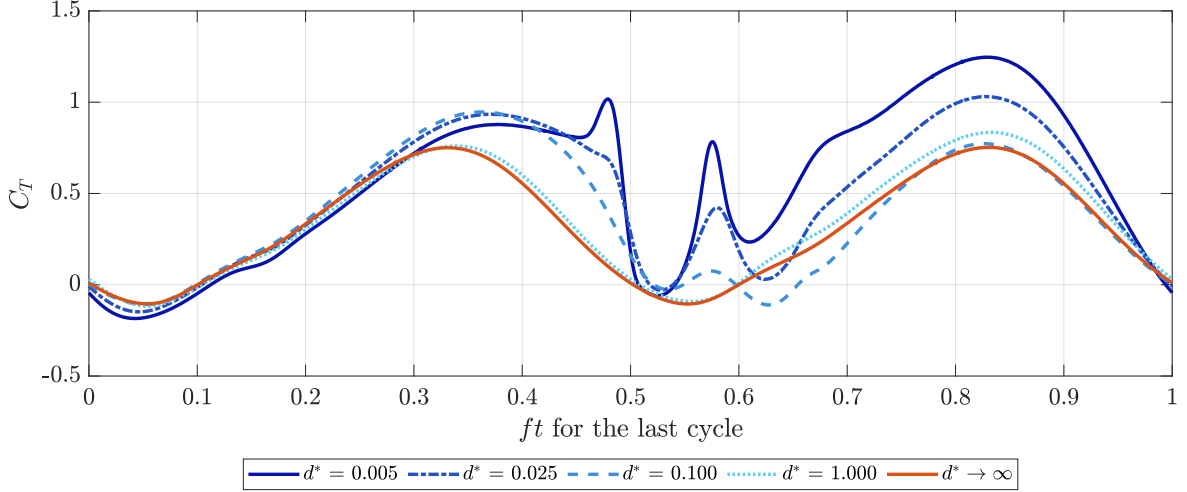


Figure 27: Comparison of the thrust coefficient  $C_T$  for  $\phi = 105^\circ$  between the single-foil case and several dual-foil cases.

#### 4.4. Deviation kinematics

Based on the results presented in Section 4.1 and Section 4.2, the kinematics of several cases with deviation are investigated. More specifically, it will be determined how different combinations of deviation amplitude  $l^*$  and phase shift between the deviation and heaving motion  $\psi$  affect the instantaneous angle of attack of the foils which

necessarily impacts the performances. Figure 28 and Figure 29 present the motion of a single foil according to different combinations of the parameters  $l^*$  and  $\psi$ . The trajectory of the pivot point position located near the leading edge at  $x_p^* = 0.005$  as well as the point located at the trailing edge are represented by the blue curves for one period of motion. As seen in Figure 28, the pivot point of a flapping foil with no deviation moves only vertically according to the heaving motion defined Section 2.1. Additionally, this baseline configuration also results in a figure-of-eight pattern for the trailing edge. When the deviation is in phase with the heaving motion, but with a reduced frequency twice as fast, the pivot point yields the same pattern as the one described by Fry et al. (2003) and Bos et al. (2008). Increasing the deviation amplitude widens this pattern and modifies the trajectory of the trailing edge, which necessarily impacts how the foils perform the clap phase when the minimum spacing  $d^*$  is reached. Next, Figure 29 shows the effect of modifying the phase shift  $\psi$  for a configuration of moderate deviation amplitude  $l_0 = 0.035$ . As seen in the figure, a positive phase shift tilts the figure-of-eight pattern of the pivot point to the right while a negative phase shift tilts it to the left. Moreover, when the phase shift is equal to  $\pm 90^\circ$  the figure of eight disappears and the trajectory becomes the same for the upstroke and the downstroke of the foil while maintaining a certain tilt. Lastly, the configuration with  $l^* = 0.035$  and  $\psi = -125^\circ$  which yielded the best efficiency presents a figure-of-eight pattern tilted to the left for the pivot point, and interestingly, the trajectory of the trailing edge becomes essentially the same for the upstroke and the downstroke. This configuration, which includes deviation, changes the evolution of the effective angle of attack of each foil but preserves a consistent trajectory of the trailing edges during the clap phase where each of them essentially moves on the same line when approaching and departing from the minimum spacing  $d^*$ .

As briefly discussed, the different motion parameters change the figure-of-eight pattern of the flapping foils thus impacting their effective velocity and angle of attack, which can modulate the aerodynamic performances. Figure 30 and Figure 31 present the evolution of instantaneous power and thrust coefficients of cases with different parameters  $l^*$  and  $\psi$ . The maximum power and thrust coefficients are obtained near the middle of the upstroke close to the beginning of the cycle, as shown in Figure 30 and Figure 31. In cases with no and moderate deviation, the peaks are similar and occur around the instant  $ft = 0.08$ . For the case with substantial deviation ( $l^* = 0.150, \psi = 40^\circ$ ), the peaks are less important and occur earlier in the cycle. This is due to the effective velocity which is out of phase in this configuration

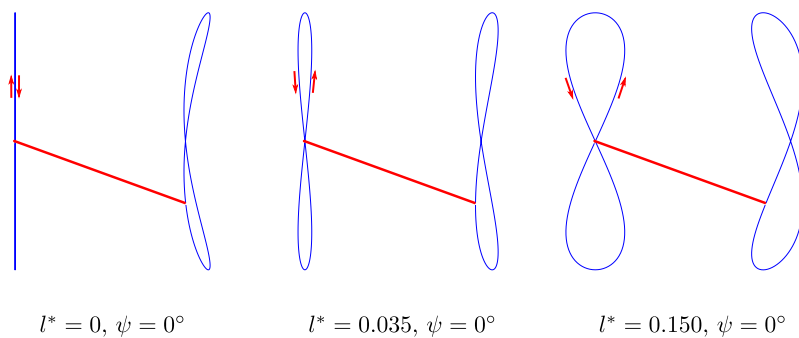


Figure 28: Baseline deviation motion ( $\psi = 0^\circ$ ) for several amplitudes  $l^*$ .

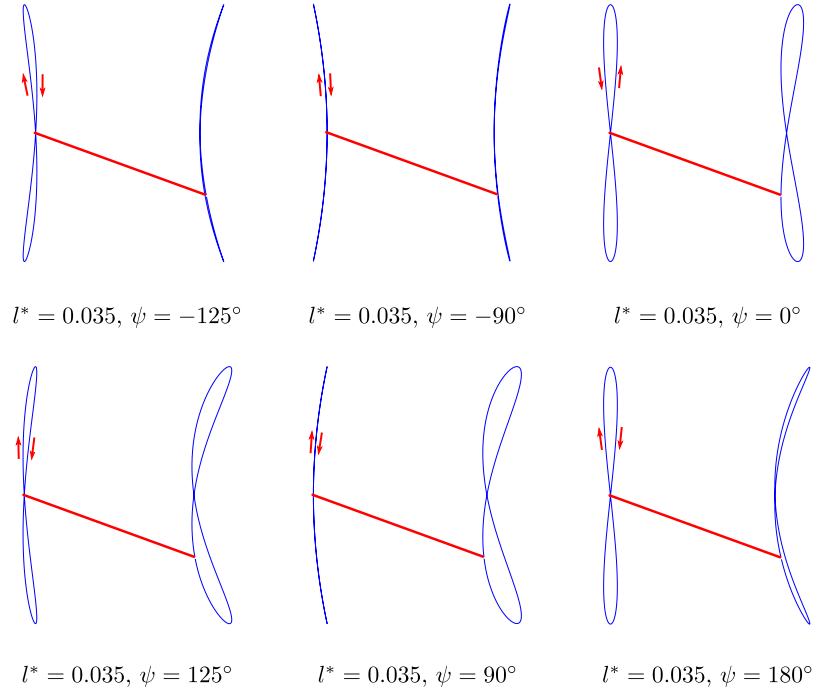


Figure 29: Deviation motion based on the best efficiency configuration ( $l^* = 0.035$ ) for several phase shifts  $\psi$ .

compared to the other cases as observed in Figure 32. This figure presents both the horizontal component of the effective velocity and the magnitude of the effective velocity which includes the vertical component related to the heaving motion of the foils (see Equation 14). Compared with the best case with deviation ( $l^* = 0.035, \psi = -125^\circ$ ), the two other reported cases with deviation exhibit effective horizontal velocity evolutions that are out of phase by  $165^\circ$ , thus almost perfectly reversing where the peaks and the troughs occur during one cycle. However, since the vertical component of the effective velocity is the same in all cases and is higher in magnitude than the horizontal one, the magnitude of the effective velocity is not as affected relative to the case without deviation for cases with a moderate amount as seen in Figure 32. Indeed, the moderate normalized deviation amplitude  $l^* = 0.035$  is a small fraction of the normalized heaving amplitude  $h^* = 1$  and thus does not alter as much the distribution of the effective velocity as the case with higher deviation with the normalized amplitude  $l^* = 0.150$ . This phase shift is also apparent in Figure 33 which presents the distribution of the effective angle of attack of the different cases. The curves of the effective angle of attack with no and moderate deviation are essentially the same, while the one with substantial deviation has a larger amplitude that occurs with a significant delay. This delay in the evolution of the effective angle of attack thus explains why the first and second power and thrust peaks observed during the upstroke and downstroke are respectively shifted. The peaks are consequently of lower magnitude due to the effective velocity which is also lower at this instant as seen in Figure 32.

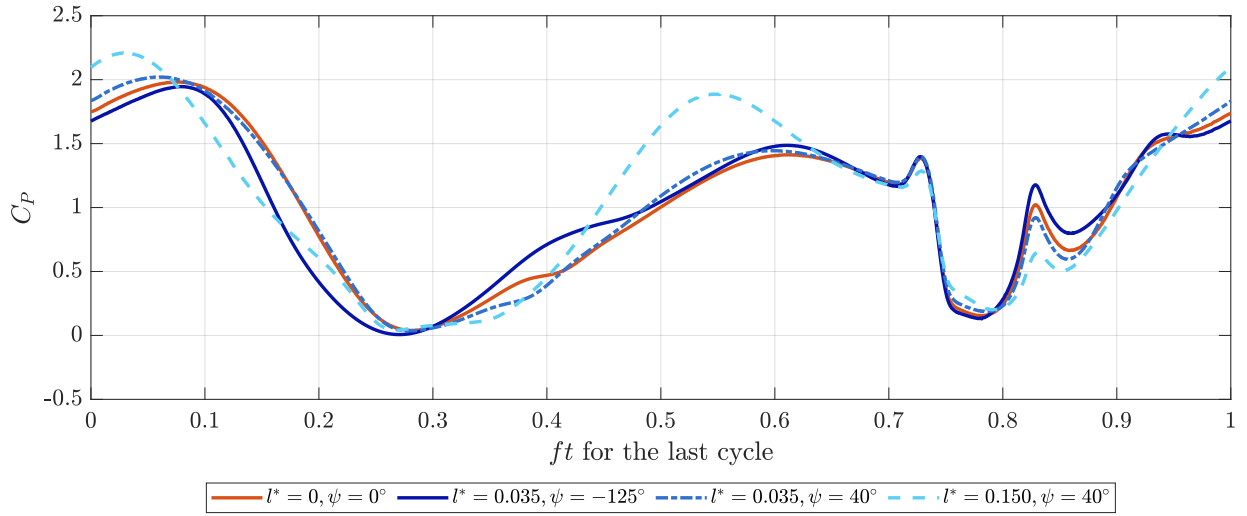


Figure 30: Comparison of the instantaneous power coefficient  $C_P$  for different combinations of  $l^*$  and  $\psi$ .

As explained previously, the first peak in the power and thrust coefficient curves is caused by the foils' acceleration after the stroke reversal occurring during the clap phase of the previous motion cycle, imparting an important impulse to the fluid which increases thrust (Sun and Tang, 2002). Afterward, the second stroke reversal of the foils occurs around  $ft = 0.30$  and the foils thus begin the downstroke of the motion. Another peak related to the foils' acceleration is observed around  $ft = 0.615$  during the downstroke, similar to one produced during the upstroke.

The last two peaks observed during the cycle are directly related to the clap-and-fling phenomenon. The one observed near  $ft = 0.729$  represents the instant where the leading edges of the foils reach proximity due to the choice

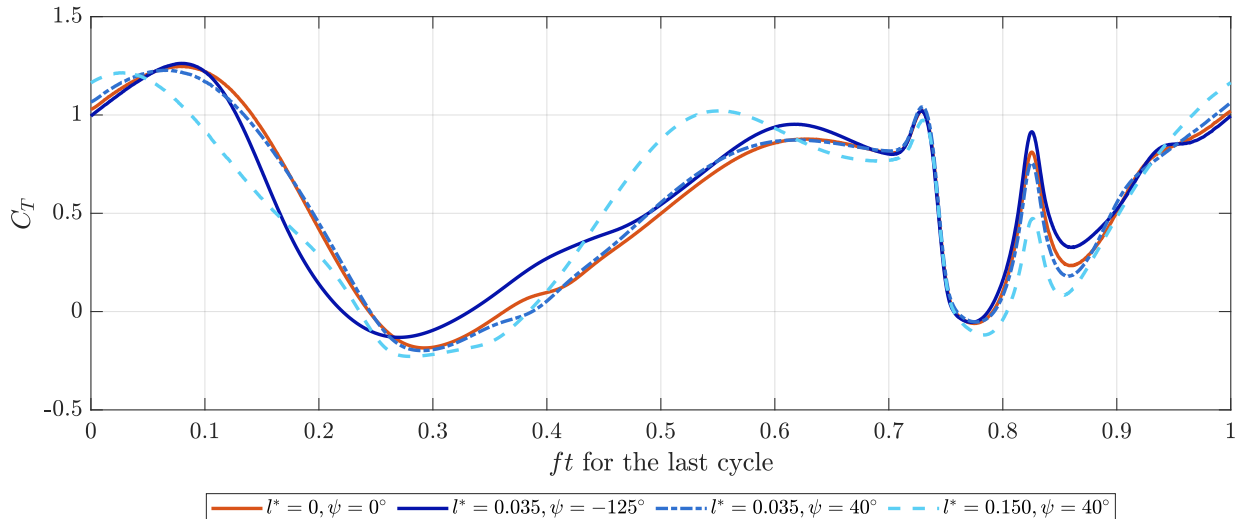


Figure 31: Comparison of the instantaneous thrust coefficient  $C_T$  for different combinations of  $l^*$  and  $\psi$ .

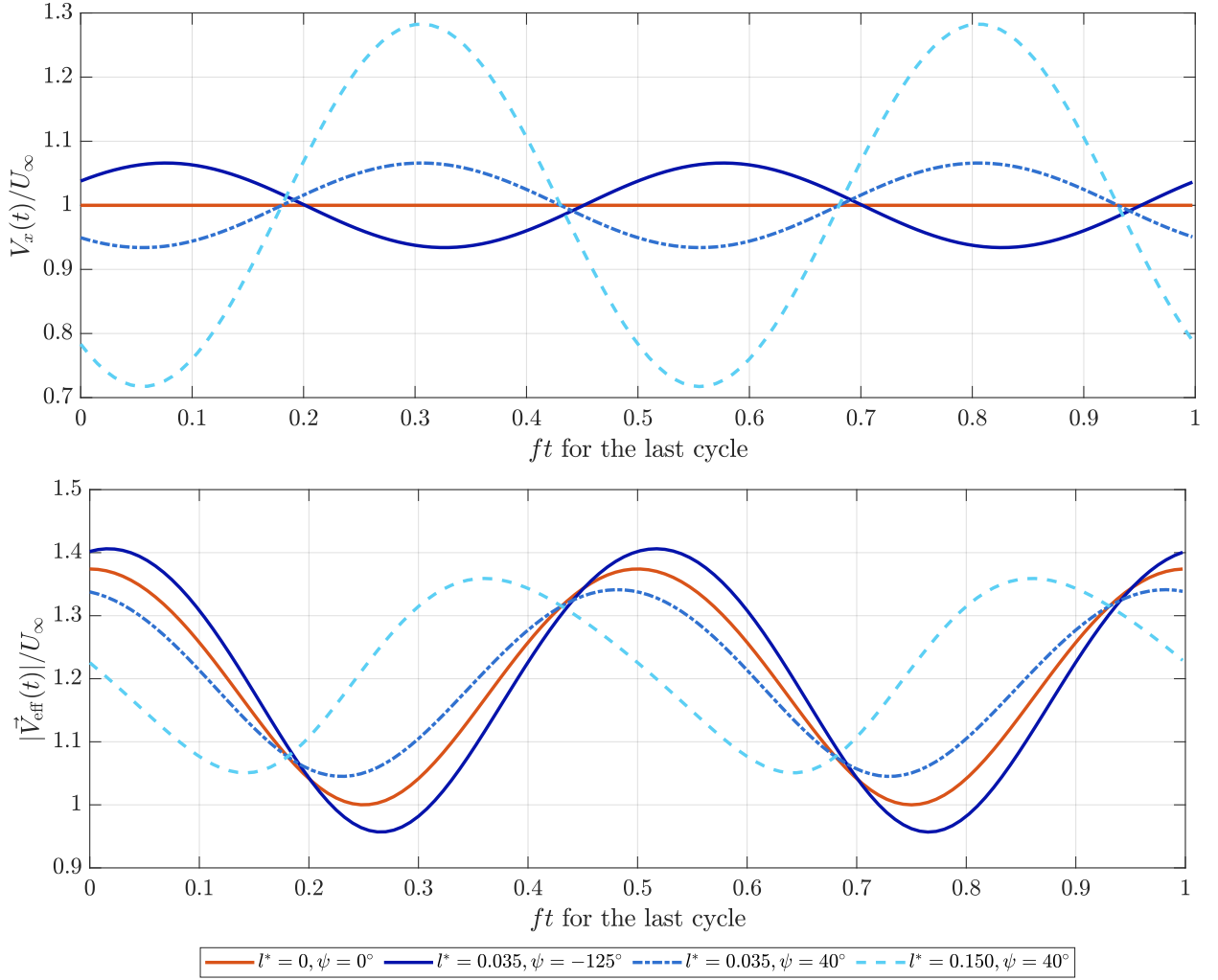


Figure 32: Horizontal component (top) and magnitude (bottom) of the effective velocity  $\vec{V}_{\text{eff}}$  for different combinations of  $l^*$  and  $\psi$ .

of proper kinematics. As explained in Section 4, the configuration with a phase shift between the heaving and pitching motion of  $\phi = 105^\circ$  generates a large positive pressure zone between the foils immediately to the right of their leading edges as they reach proximity. The resulting pressure gradient between the zones upstream and downstream of the leading edges of the foils thus produces an important local thrust peak. Figure 31 shows that this thrust peak is not strongly affected by the different configurations where deviation is present. At this instant, the effective angles of attack of all cases are practically identical, while the effective velocities present important differences, as seen in Figure 32 and Figure 33. Thus, it can be concluded that changing the effective velocity does not strongly influence the thrust and power coefficient curves.

The last thrust peak which results directly from the clap-and-fling mechanism, as explained in Section 4, occurs at  $ft = 0.826$ . It is observed that the maximum value of the baseline case reported on Figure 31 ( $C_T = 0.78$ ) is affected

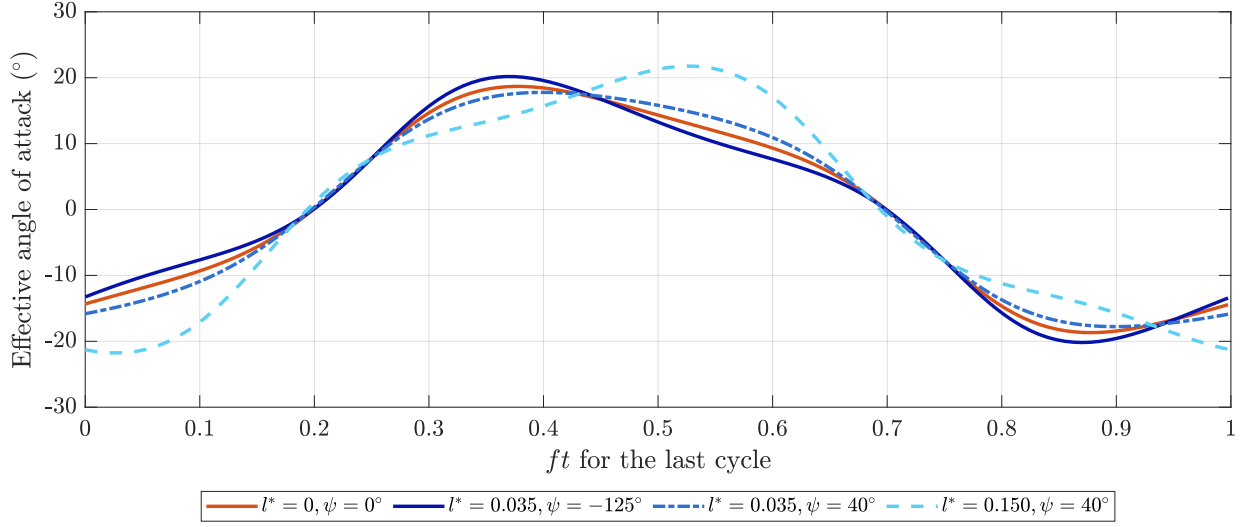


Figure 33: Effective angle of attack for different combinations of  $l^*$  and  $\psi$ .

by the deviation component of the motion. Indeed, the optimal case with moderate deviation ( $l^* = 0.035, \psi = -125^\circ$ ) increases this thrust peak to  $C_T = 0.915$ . At this instant, this case has a lower effective velocity than the baseline case without deviation, as seen on Figure 32. However, it was previously mentioned that the effective velocity has little impact on performance. On the other hand, the effective angles of attack are different at this instant. Indeed, the configuration without deviation presents a value of  $-16.93^\circ$ , while the optimal case with moderate deviation yields one of  $-18.37^\circ$ . This increase, slightly higher than  $1^\circ$ , of the effective angle of attack thus significantly modulates the instantaneous performance metrics, especially the thrust coefficient. The lowest value of effective angle of attack at  $ft = 0.826$  is for the case with the most important tested deviation amplitude ( $l^* = 0.150, \psi = 40^\circ$ ). This low angle of attack ( $\alpha = -12.32^\circ$ ) significantly decreases the thrust coefficient to  $C_T = 0.47$ . Thus, a proper phase shift between heaving and deviation  $\psi$  can accentuate the beneficial unsteady effects yielded by the clap-and-fling mechanism through the modulation of the effective angle of attack. For example, the thrust peaks obtained when the foils are close to each other during the clap phase can be increased substantially. It was also shown that the deviation amplitude  $l^*$  also greatly impacts the effective velocity as well as the effective angle of attack of the foils during a cycle of motion, which is beneficial for moderate values and impairs the flow for greater values such as  $l^* = 0.150$ .

## 5. Conclusion

This study investigated oscillating foils employing the clap-and-fling mechanism to generate thrust. Two-dimensional numerical simulations were conducted at a Reynolds number of 800, with plate-shaped foils exhibiting sinusoidal pitching, heaving, and deviation motions. Different phase shifts between these motions were tested in the simulations. Two parametric studies, without and with deviation, were performed at a reduced frequency of 0.15, ensuring periodic and highly efficient results. In this regime, rapid convection of leading-edge vortices in the wake prevents strong

interaction with the two foils. The main objectives of this study were first to characterize efficiency improvements obtained through the clap-and-fling mechanism and to determine if the thrust could also be increased. Second, the study aimed to determine if implementing the deviation motion in a system subjected to the clap-and-fling mechanism with optimized kinematics could further increase both thrust and efficiency.

In cases without deviation, significant thrust and efficiency improvements were obtained by reducing the minimum spacing between the foils and adjusting the phase shift between the heaving and pitching motions. The best case produced a 0.542 efficiency and a thrust coefficient of 0.549. This occurred with a phase shift of  $105^\circ$  and with a minimum spacing such that the two foils almost touch at the trailing edge. This high-efficiency configuration represents a significant improvement when compared to the best case of a single oscillating foil which provided an efficiency of 0.478 at a phase shift of  $\phi = 105^\circ$  and a thrust coefficient of 0.36 at  $\phi = 110^\circ$ . In the best case previously reported, this minimum spacing occurred at the trailing edge during the motion of the foils, and it produced a low-pressure zone to their upstream side due to the entrapment of the fluid between the two foils, which resulted in a significant peak of thrust during the cycle at this instant. Similarly, a high-pressure zone was observed between the foils downstream of the leading edges as they come close to each other, which increases thrust and efficiency. However, it was shown that this ideal scenario, where the pressure gradient is favorable to the thrust production at a low minimum spacing, is very sensitive to the phase shift. For example, increasing the phase shift to  $110^\circ$  caused the minimum spacing to occur at the leading edge instead of the trailing edge, decreasing both the thrust and the efficiency.

Further enhancements were achieved by including the deviation motion and adjusting its amplitude and phase shift. In the most favorable configuration, a remarkable 0.560 efficiency and an averaged thrust coefficient of 0.563 were obtained. This optimal configuration, with a phase shift of  $\psi = -125^\circ$  and a moderate deviation amplitude of  $l^* = 0.035$ , produced increases of 17.14% in efficiency and 56.39% in thrust coefficient compared to the best single-foil case. Implementing the deviation motion thus accentuates the beneficial effects of the minimum spacing by favorably modulating the effective angle of attack experienced by the foils near the thrust peak. Moreover, the reported propulsive standard deviation was  $\sigma_{C_T} = 0.412$ . This represents a slight decrease compared to the base case without deviation ( $\sigma_{C_T} = 0.429$ ) indicating less transient force variations during the motion. However, increasing thrust solely through deviation comes at the cost of having a slightly greater force variations throughout the motion.

Even though the wing kinematics studied in this work does not directly represent the three-dimensional wing motions observed in flying species, it illustrates that a simpler in-plane flapping motion exhibits similar benefits when combined with deviation and clap-and-fling kinematics. By using high-aspect-ratio wings that would mitigate 3D effects, the kinematics described in this paper could thus be used as a viable mechanical system to produce thrust. Nevertheless, the exploration of three-dimensional effects could be undertaken through comparable yet more extensive computational fluid dynamics simulations. This would allow their influence on the clap-and-fling phenomenon to be quantified. These effects are relevant to the current in-plane kinematics and to the more intricate three-dimensional motions observed in nature.

## References

- J. M. Anderson, K. Streitlien, D. S. Barrett, and M. S. Triantafyllou. Oscillating foils of high propulsive efficiency. *Journal of Fluid Mechanics*, 360:41–72, April 1998. ISSN 0022-1120, 1469-7645. doi: 10.1017/S0022112097008392.
- S.A. Ansari, R. Żbikowski, and K. Knowles. Aerodynamic modelling of insect-like flapping flight for micro air vehicles. *Progress in Aerospace Sciences*, 42(2):129–172, February 2006. ISSN 03760421. doi: 10.1016/j.paerosci.2006.07.001.
- Akira Azuma. *The biokinetics of flying and swimming*. AIAA education series. American Institute of Aeronautics and Astronautics, Inc, Reston, VA, 2nd ed edition, 2006. ISBN 978-1-56347-781-2. OCLC: ocm69423258.
- Frank M. Bos, D. Lentink, B. W. Van Oudheusden, and H. Bijl. Influence of wing kinematics on aerodynamic performance in hovering insect flight. *Journal of Fluid Mechanics*, 594:341–368, January 2008. ISSN 0022-1120, 1469-7645. doi: 10.1017/S0022112007009172.
- Long Chen, Jianghao Wu, and Bo Cheng. Leading-edge vortex formation and transient lift generation on a revolving wing at low Reynolds number. *Aerospace Science and Technology*, 97:105589, February 2020. ISSN 12709638. doi: 10.1016/j.ast.2019.105589.
- Long Chen, Chao Zhou, Nathaniel H. Werner, Bo Cheng, and Jianghao Wu. Dual-stage radial–tangential vortex tilting reverses radial vorticity and contributes to leading-edge vortex stability on revolving wings. *Journal of Fluid Mechanics*, 963:A29, May 2023. ISSN 0022-1120, 1469-7645. doi: 10.1017/jfm.2023.196.
- Michael H. Dickinson, Fritz-Olaf Lehmann, and Sanjay P. Sane. Wing rotation and the aerodynamic basis of insect flight. *Science*, 284(5422): 1954–1960, June 1999. ISSN 0036-8075, 1095-9203. doi: 10.1126/science.284.5422.1954.
- Charles P. Ellington, Coen van den Berg, Alexander P. Willmott, and Adrian L. R. Thomas. Leading-edge vortices in insect flight. *Nature*, 384 (6610):626–630, December 1996. ISSN 0028-0836, 1476-4687. doi: 10.1038/384626a0.
- Steven N. Fry, Rosalyn Sayaman, and Michael H. Dickinson. The Aerodynamics of Free-Flight Maneuvers in *Drosophila*. *Science*, 300(5618): 495–498, April 2003. ISSN 0036-8075, 1095-9203. doi: 10.1126/science.1081944.
- K. Isogai, Y. Shinmoto, and Y. Watanabe. Effects of dynamic stall on propulsive efficiency and thrust of flapping airfoil. *AIAA Journal*, 37(10): 1145–1151, 1999. doi: 10.2514/2.589.
- K.D. Jones and M.F. Platzer. Design and development considerations for biologically inspired flapping-wing micro air vehicles. *Experiments in Fluids*, 46:799–810, 2009. doi: 10.1007/s00348-009-0654-1.
- Hyunwoo Jung, Sehyeong Oh, and Haechon Choi. Role of the deviation motion on the aerodynamic performance of a mosquito wing in hover. *Computers & Fluids*, 270:106146, February 2024. ISSN 00457930. doi: 10.1016/j.compfluid.2023.106146.
- M. J. Lighthill. On the Weis-Fogh mechanism of lift generation. *Journal of Fluid Mechanics*, 60(1):1–17, August 1973. ISSN 0022-1120, 1469-7645. doi: 10.1017/S0022112073000017.
- Sun Mao and Yu Xin. Flows around two airfoils performing fling and subsequent translation and translation and subsequent clap. *Acta Mechanica Sinica*, 19(2):103–117, April 2003. ISSN 0567-7718, 1614-3116. doi: 10.1007/BF02487671.
- Laura A. Miller and Charles S. Peskin. A computational fluid dynamics of ‘clap and fling’ in the smallest insects. *Journal of Experimental Biology*, 208(2):195–212, January 2005. ISSN 1477-9145, 0022-0949. doi: 10.1242/jeb.01376.
- Mathieu Olivier. *A fluid-structure interaction partitioned algorithm applied to flexible flapping wing propulsion*. PhD thesis, Université Laval, 2014.
- Mathieu Olivier and Guy Dumas. A parametric investigation of the propulsion of 2D chordwise-flexible flapping wings at low Reynolds number using numerical simulations. *Journal of Fluids and Structures*, 63:210–237, May 2016. ISSN 08899746. doi: 10.1016/j.jfluidstructs.2016.03.010.
- Max Platzer, Kerrin Neace, and Chung-Kiang Pang. Aerodynamic analysis of flapping wing propulsion. In *31st Aerospace Sciences Meeting*, Reno, NV, U.S.A., January 1993. American Institute of Aeronautics and Astronautics. doi: 10.2514/6.1993-484.
- Max F. Platzer, Kevin D. Jones, John Young, and Joseph C. S. Lai. Flapping wing aerodynamics: Progress and challenges. *AIAA Journal*, 46(9): 2136–2149, September 2008. ISSN 0001-1452, 1533-385X. doi: 10.2514/1.29263.
- Sanjay P. Sane. The aerodynamics of insect flight. *Journal of Experimental Biology*, 206(23):4191–4208, December 2003. ISSN 1477-9145, 0022-0949. doi: 10.1242/jeb.00663.

- Wei Shyy, Yongsheng Lian, Jian Tang, Dragos Viieru, and Hao Liu. *Aerodynamics of Low Reynolds Number Flyers*. Cambridge University Press, 1 edition, October 2007. ISBN 978-0-521-20401-9 978-0-521-88278-1 978-0-511-55115-4. doi: 10.1017/CBO9780511551154.
- M. Sun and J. Tang. Unsteady aerodynamic forces in a flapping model wing. *The Journal of Experimental Biology*, pages 55–70, 2002.
- Bret W. Tobalske, Douglas R. Warrick, Christopher J. Clark, Donald R. Powers, Tyson L. Hedrick, Gabriel A. Hyder, and Andrew A. Biewener. Three-dimensional kinematics of hummingbird flight. *Journal of Experimental Biology*, 210(13):2368–2382, July 2007. ISSN 1477-9145, 0022-0949. doi: 10.1242/jeb.005686.
- Ismail Tuncer and Max Platzer. A computational study of flow separation characteristics and wake profiles behind a flapping airfoil. In *37th Aerospace Sciences Meeting and Exhibit*, Reno, NV, U.S.A., January 1999. American Institute of Aeronautics and Astronautics. doi: 10.2514/6.1999-648.
- Kamal Viswanath and Danesh K. Tafti. Effect of Stroke Deviation on Forward Flapping Flight. *AIAA Journal*, 51:145–160, January 2013. ISSN 0035-7529, 1940-1191. doi: 10.2514/1.J051675.
- Z. Jane Wang, James M. Birch, and Michael H. Dickinson. Unsteady forces and flows in low Reynolds number hovering flight: two-dimensional computations vs robotic wing experiments. *Journal of Experimental Biology*, 207(3):449–460, January 2004. ISSN 1477-9145, 0022-0949. doi: 10.1242/jeb.00739.
- Torkel Weis-Fogh. Quick estimates of flight fitness in hovering animals, including novel mechanisms for lift production. *Journal of Experimental Biology*, 59(1):169–230, 08 1973. ISSN 0022-0949. doi: 10.1242/jeb.59.1.169.
- Xia Wu, Xiantao Zhang, Xinliang Tian, Xin Li, and Wenyue Lu. A review on fluid dynamics of flapping foils. *Ocean Engineering*, 195:106712, January 2020. ISSN 0029-8018. doi: 10.1016/j.oceaneng.2019.106712.
- Jianyang Zhu and Bin Lei. Effect of Wing-Wing Interaction on the Propulsive Performance of Two Flapping Wings at Biplane Configuration. *Applied Bionics and Biomechanics*, 2018:1–12, September 2018. ISSN 1176-2322, 1754-2103. doi: 10.1155/2018/8901067.